



# Recrystallization in non-conventional microstructures of 316L stainless steel produced via laser powder-bed fusion: effect of particle coarsening kinetics

F. C. Pinto<sup>1</sup>, L. S. Aota<sup>1,2,\*</sup> , I. R. Souza Filho<sup>2</sup>, D. Raabe<sup>2</sup>, and H. R. Z. Sandim<sup>1</sup>

<sup>1</sup>Lorena School of Engineering, University of Sao Paulo, Lorena, SP 12602-810, Brazil

<sup>2</sup>Max-Planck-Institut für Eisenforschung, 40237 Düsseldorf, Germany

Received: 25 August 2021

Accepted: 30 December 2021

© The Author(s) 2022

## ABSTRACT

Alloys processed by laser powder-bed fusion show distinct microstructures composed of dislocation cells, dispersed nanoparticles, and columnar grains. Upon post-build annealing, such alloys show sluggish recrystallization kinetics compared to the conventionally processed counterpart. To understand this behavior, AISI 316L stainless steel samples were constructed using the island scan strategy. Rhodonite-like ( $\text{MnSiO}_3$ ) nanoparticles and dislocation cells are found within weakly-textured grains in the as-built condition. Upon isothermal annealing at 1150 °C (up to 2880 min), the nucleation of recrystallization occurs along the center of the melt pool, where nuclei sites, high stored elastic energy, and local large misorientation are found in the as-built condition. The low value of the Avrami coefficient ( $n = 1.16$ ) can be explained based on the non-random distribution of nucleation sites. The local interaction of the recrystallization front with nanoparticles speeds up their coarsening causing the decrease of the Zener-Smith pinning force. This allows the progression of recrystallization in LPBF alloys, although sluggish. These results allow us to understand the progress of recrystallization in LPBF 316L stainless steel, shedding light on the nucleation mechanisms and on the competition between driving and dragging pressures in non-conventional microstructures. They also help to understand the most relevant microstructural aspects applicable for tuning microstructures and designing new LPBF alloys.

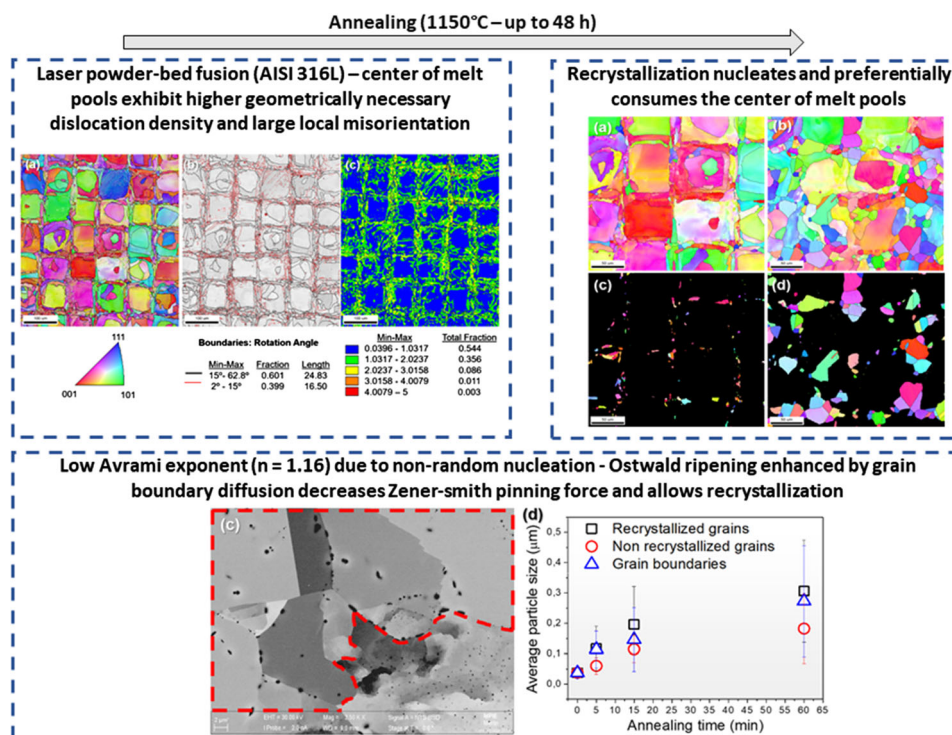
Handling Editor: M. Grant Norton.

Address correspondence to E-mail: l.aota@mpie.de; leonardoaota@usp.br

<https://doi.org/10.1007/s10853-021-06859-1>

Published online: 20 January 2022

## GRAPHICAL ABSTRACT



## Introduction

Additive manufacturing (AM) consists of the repeated deposition and melting of a feedstock in a layer-by-layer iterative process until the final part is achieved. In this process, a broad range of metallic materials has been studied and applied in the industry. Among the existing AM techniques for such materials, laser powder-bed fusion (LPBF) has been attracting great interest due to the possibility of printing near-net-shape parts with complex geometries [1–3]. By adjusting the laser beam power [4], the powder layer thickness and the scan strategy [5, 6], microstructures can be tailored to achieve enhanced properties.

The engineered microstructures of LPBF materials are unique [7–9] compared to their wrought counterparts. At the mesoscopic level, they consist of several melt pools with a size of tens of micrometers containing columnar grains where regular dislocation

cell structures are embedded. Another general feature is the presence of an unintended dispersion of nanoparticles in the matrix, most oxides, as reported in several metal systems [10–14].

An interesting phenomenon to further tailor LPBF microstructures is recrystallization, which is obtained by post-processing annealing. The driving force for recrystallization is the elastic energy stored in the dislocation cell walls formed due to the elevated thermal strains imposed by the high cooling rates and the subsequent alternating heating and cooling cycles [3, 15–22]. Post-build annealing behavior of LPBF-processed materials has been reported in the literature [3, 14, 23–38], where the final microstructure or the modification of mechanical or electrochemical properties following annealing have been investigated.

While texture evolution is fairly well understood during LPBF processing [39–41], only a few works have addressed the mesoscale texture evolution [26, 42–44] and the texture evolution [29, 42, 45] in

LPBF-processed materials upon annealing. Therefore, key aspects such as those determining the underlying nucleation mechanisms, the competition between driving and dragging pressures, and recrystallization kinetics have been rarely reported. Most works cited above refer to the AISI 316L stainless steel, while the remaining ones refer to Ni-based superalloys. Only two works focus on the recrystallization mechanisms in AISI 316L and IN718 alloys in detail [45, 46], where their sluggish kinetics have been assigned to the interaction of high angle boundaries with oxide/silicate nanoparticles. Therefore, further investigations are required to understand whether the microstructure evolution and the recrystallization mechanisms are similar between samples from different alloys or obtained under different LPBF processing conditions.

In the present work, the aforementioned gaps in the literature were addressed to understand the recrystallization kinetics in LPBF alloys. In particular, this work quantifies nanoparticle coarsening due to their interaction with the recrystallization front and its effect on the sluggish recrystallization kinetics in LPBF AISI 316L stainless steel. To this end, the classical Johnson–Mehl–Avrami–Kolmogorov (JMAK) model was applied to estimate the recrystallization kinetics (Avrami exponent). The underlying recrystallization mechanisms in metallic parts produced by LPBF additive manufacturing are revealed, allowing to tune the microstructure during or after the building process.

## Experimental

### Material

The starting material is an AISI 316L austenitic stainless-steel CL-20 reused powder batch with spherical particles produced by Concept Laser GmbH. The mean particle size was 26  $\mu\text{m}$ . The chemical composition of AISI 316L steel in the as-built condition is shown in Table 1. Bulk samples were manufactured as cylinders ( $\phi 15\text{ mm} \times 50\text{ mm}$ ) using a Mlab Cusing R machine under nitrogen atmosphere. The parts were produced using the island scan strategy where the layer is divided into smaller squares of size  $5 \times 5\text{ mm}^2$  and the laser scanning direction rotates  $90^\circ$  between both every island and layer, as depicted in Fig. 1. The main processing parameters used in LPBF were the

**Table 1** Chemical composition of AISI 316L stainless steel cylinders processed by LPBF in the present investigation (in wt%)

C	Cr	Ni	Mo	Mn	Si	N
0.0233	16.5819	10.066	2.0846	1.3028	0.4965	0.09
O	V	W	Nb	Cu	Co	Fe
0.07	0.0724	0.0592	0.0191	0.3065	0.1772	Bal.

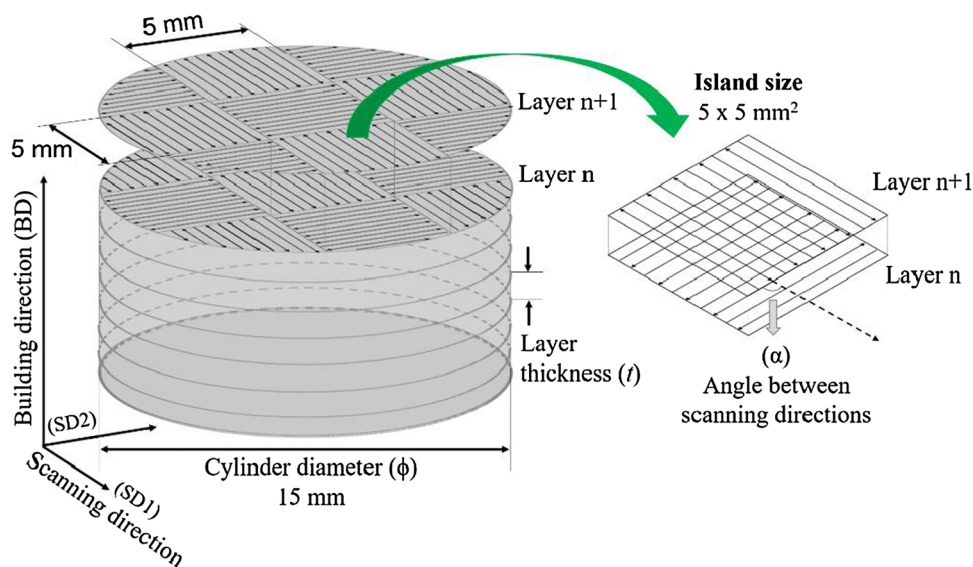
following: laser power ( $P$ ) of 90 W, layer thickness ( $t$ ) of 30  $\mu\text{m}$ , hatch distance ( $d_H$ ) of 90  $\mu\text{m}$ , and scanning velocity ( $v$ ) 1500 mm/s. Further details about this manufacturing protocol can be found in a preceding work [47].

### Annealing and microstructural characterization

The LPBF samples were isothermally annealed in vacuum-sealed quartz tubes at 1150  $^\circ\text{C}$  from 5 min up to 2880 min (48 h), followed by water cooling. Thermodynamic simulations were performed using the software Thermo-Calc<sup>TM</sup> coupled with the TCFE-9 database to determine the phase stability diagram of this steel, thus helping us to understand the formation of silicate/oxide nanoparticles from the liquid and to select the optimal annealing temperature within the austenite single-phase field.

Metallographic sections taken parallel and perpendicular to the build direction (BD) were prepared by conventional metallography. Electrolytic etching was performed in an aqueous 10% oxalic acid solution at 5.0 V for 90 s for the acquisition of images in a Leica DM-IRM light optical microscope. Electron channeling contrast imaging was performed in a Zeiss Merlin scanning electron microscope (SEM) operating at 30 kV. EBSD maps were acquired on both the build plane ( $SD1 \times SD2$ ) and along a section parallel to the BD of the as-built samples, whereas only the  $SD1 \times SD2$  plane was analyzed on annealed samples. Here, SD stands for the scanning direction, as shown in Fig. 1. For this purpose, we used a JEOL JSM-6500F SEM, coupled with a DigiView EBSD detector from EDAX/Ametek with a step size of 700 nm and an accelerating voltage of 15 kV at a working distance of 18 mm. All pixels with confidence index (CI) below 0.1 were removed from the dataset. Grain orientation spread (GOS) maps were used to determine the recrystallized grains assuming

**Figure 1** Schematic diagram showing the main characteristics of LPBF samples. The arrows indicate the movement of the laser source and  $\alpha$  is the rotation angle of the scanning direction between the consecutive layers  $n$  and  $n + 1$ . SD1 and SD2 are equivalent due to the  $90^\circ$  rotation between layers.



a  $\text{GOS} \leq 1^\circ$  criterion, considering grain boundaries as interfaces with misorientation higher than  $5^\circ$  and a minimum recrystallized grain size of  $2 \mu\text{m}$ . Kernel average misorientation (KAM) maps were constructed using the 3<sup>rd</sup> nearest neighbor with a  $5^\circ$  tolerance angle to reveal the misorientation gradients developed within the microstructures after the LPBF process as well as their changes upon annealing. Contoured pole figures (PF) were calculated using a discrete binning method.

Vickers hardness testing was performed using a load of 200 g for 30 s parallel to the scanning direction (SD1  $\times$  SD2) in a total number of 15 individual measurements. X-ray diffraction (XRD) measurements were conducted in the as-built specimen on the SD1  $\times$  SD2 section using a Seifert Type ID3003 diffractometer equipped with a  $\text{Co-K}\alpha$  radiation source and operated at 40 kV and 30 mA. The sample was measured under rotation around the build direction (BD) under an angular speed of  $\pi \text{ s}^{-1}$ . The diffracted data were acquired in the  $2\theta$  range between  $30$  and  $120^\circ$  with angular steps of  $0.03^\circ$  and a dwell time of 10 s. The obtained data were analyzed by means of a Rietveld-based refinement methodology using the software MAUD (*Materials Analysis Using Diffraction*) [48, 49]. The Popa model for size-strain analysis was also used to evaluate the effective crystallite portions ( $D_{\text{eff}}$ ), responsible for diffracting the X-ray radiation, and the magnitude of the accumulated microstrain  $\langle \varepsilon_{\text{hh}}^2 \rangle^{1/2}$  in austenite [50]. The Popa method is implemented in the software MAUD and the reliability of the refinements was

established by the goodness of fit (GoF) parameter, which must converge to the unity for an optimal fit [51, 52].

The overall dislocation density ( $\rho$ ) was estimated according to the procedure proposed by Williamson and Smallman [53] using Eq. 1:

$$\rho = \left( \frac{3 \cdot K \cdot \langle \varepsilon_{\text{hh}}^2 \rangle}{D_{\text{eff}}^2 \cdot b^2} \right)^{1/2} \quad (1)$$

where  $K = 16.6$  for austenite (fcc) [53];  $b$  is the magnitude of the Burgers vector, which is equivalent to  $a/\sqrt{2}$  along the  $\langle 110 \rangle$  directions of the fcc structure, where  $a$  is the lattice parameter.  $D_{\text{eff}}$  and  $\langle \varepsilon_{\text{hh}}^2 \rangle^{1/2}$  are, respectively, the effective crystallite size and the accumulated microstrain.

The size distribution of the nanoparticles was determined using an image analysis routine based on SEM micrographs and the Image J software. A total number of about 25,000 particles was considered to determine their size and volume fraction. Porosity was determined using the same image analysis procedure for light optical micrographs collected from the unetched material.

## Results and discussion

### As-built condition

Samples are dense and have a porosity of  $0.28 \pm 0.15\%$ . We employed a combinatorial approach using the stability phase diagram calculation and

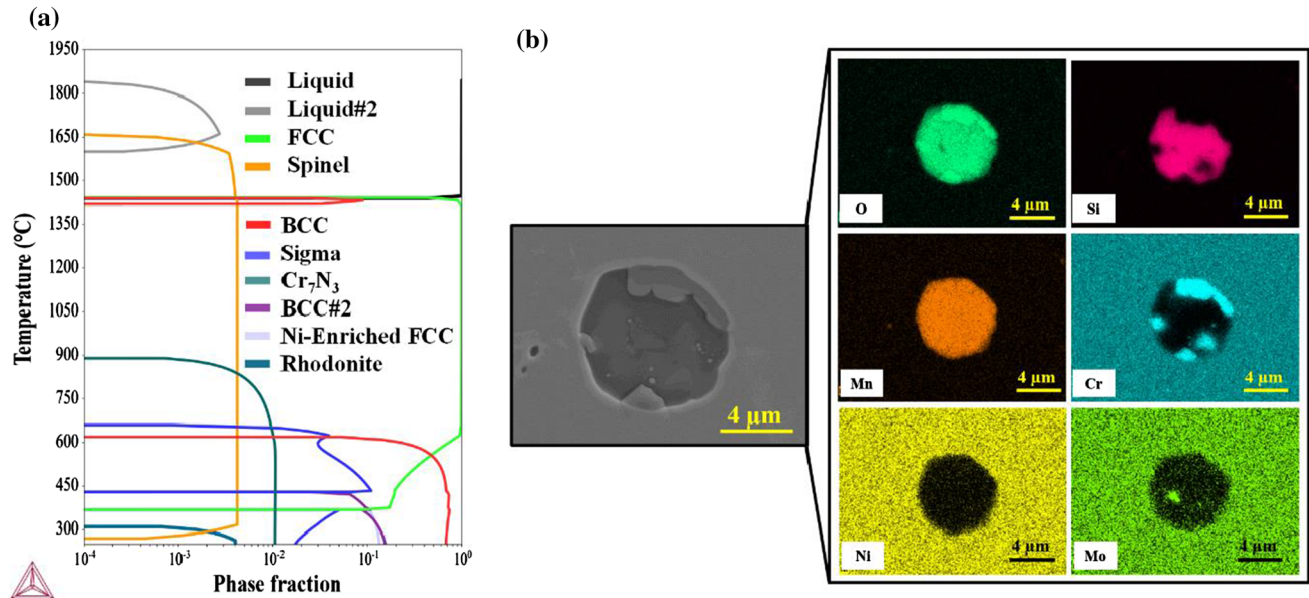


**Figure 2** **a** Thermo-Calc © equilibrium simulations for AISI 316L austenitic stainless steel showing the volume phase fractions as a function of the temperature; **b** Coarse particle obtained after

microstructural observations to understand the solidification path of LPBF 316L stainless steel and the resulting microstructure. Special focus was placed on the particle formation.

The stability phase diagram shown in Fig. 2a reveals a miscibility gap between two liquids at high temperatures; i.e., a Fe-enriched portion (namely LIQUID in Fig. 2a) that solidifies into austenite at 1450 °C, and a second one that is enriched in Si and O (namely LIQUID #2 in Fig. 2a), which solidifies as manganese silicate nanoparticles at 1600 °C. The formation of these amorphous manganese silicate in the powder feedstock occurs in the precursor gas atomization process [54]. In the LPBF process, these nanoparticles dissociate and re-nucleate during the fast solidification, further reducing their size.

The formation of these silicate nanoparticles in the precursor powder occurs due to the high affinity of silicon and manganese with oxygen. The oxygen concentration is further increased upon LPBF due to the residual concentration of oxygen in the processing chamber [54]. The fast spinodal decomposition kinetics associated with these liquids allows their separation, even under the high cooling/solidification rates imposed by the gas atomization/LPBF process. However, the degree of separation of these liquids is dependent on the cooling rate [55]. In our case, the Si–O-enriched liquid solidifies first into

an isothermal annealing at 1150° for 48 h showing the interior enriched in Mn and Si as well as a diffusion front enriched in Cr.

spherical particles whose morphology is explained by the decrease of surface area prior to solidification. The high solidification rates in gas atomization process and LPBF lead to short time for liquid separation, yielding amorphous and nanosized particles [23, 56–58]. Thus, under such solidification conditions, one may expect that the equilibrium manganese chromate spinel ( $\text{MnCr}_2\text{O}_4$ ) predicted in Fig. 2a would not be readily formed. Instead, the non-equilibrium amorphous rhodonite-like silicate ( $\text{MnSiO}_3$ ) is the most plausible stoichiometry for the particles visualized in our steel [14]. The Fe-enriched liquid portion undergoes dynamic supercooling due to the high cooling rates [49], leading its solidification to start and finish within the temperatures of the austenite stability field. Other minor phases such as  $\text{M}_{23}\text{C}_6$ ,  $\text{Cr}_7\text{N}_3$ , and sigma ( $\sigma$ ) are also predicted to occur in the equilibrium phase diagram of Fig. 2. However, despite being thermodynamically predicted, they were not experimentally observed in this work because of the high cooling rates employed during the process, thus hindering their formation. MnS is a detrimental inclusion observed in conventionally processed AISI 316L [59]. They are neither thermodynamically predicted nor experimentally observed in this study and they were also not reported in the work by Kong et al. [36].

To assess the relative chemical composition of the nanoparticles in our steel, we monitored their stability by tracking their qualitative chemical composition changes after isothermal annealing for 48 h at 1150 °C using EDS as reported in Fig. 2b. For this purpose, a coarse particle was chosen to minimize the iteration of the primary electron beam with the matrix during EDS mapping. Figure 2b shows that the interior of this particle is enriched in Mn and Si, resembling the rhodonite ( $\text{MnSiO}_3$ ) constituent predicted in Fig. 2a, similarly to the reported in the literature for the as-built 316L steel [11, 23, 56, 57, 60, 61]. Yet, Fig. 2b reveals a diffusion front enriched in Cr and O that partially consumes the original manganese silicate from its surface towards the interior. This result suggests the ongoing transformation of the amorphous  $\text{MnSiO}_3$  into the corresponding stable crystalline spinel ( $\text{MnCr}_2\text{O}_4$ ) variant, as predicted in Fig. 2a. However, the formation of other phases cannot be discarded, and only high-resolution transmission electron microscopy (HRTEM) can clarify this issue. Therefore, we have chosen to refer to these second-phase particles as (nano)particles when discussing about the annealed microstructure, as we are unable to unambiguously identify their structure. The particle volume percentage was determined as  $0.25 \pm 0.11\%$  using quantitative image analysis and fairly agrees with both, the predicted percentage of 0.4% shown in Fig. 2b and the results reported by Chao et al. [62].

Figure 3a–d show the as-built microstructures visualized in different construction sections, i.e., parallel and perpendicular to the BD. The top view ( $\text{SD1} \times \text{SD2}$ ) is shown in Fig. 3a–b, where a cross-like structure (chessboard pattern) is noticed due to the 90° rotation after every built layer [63–65]. In contrast, stacks of melt pools resembling “fish scales” [10, 66] are observed on the  $\text{BD} \times \text{SD1}$  section (Fig. 3c, d). The schematic sketch depicted in Fig. 3e shows how this peculiar microstructure forms in top and side views.

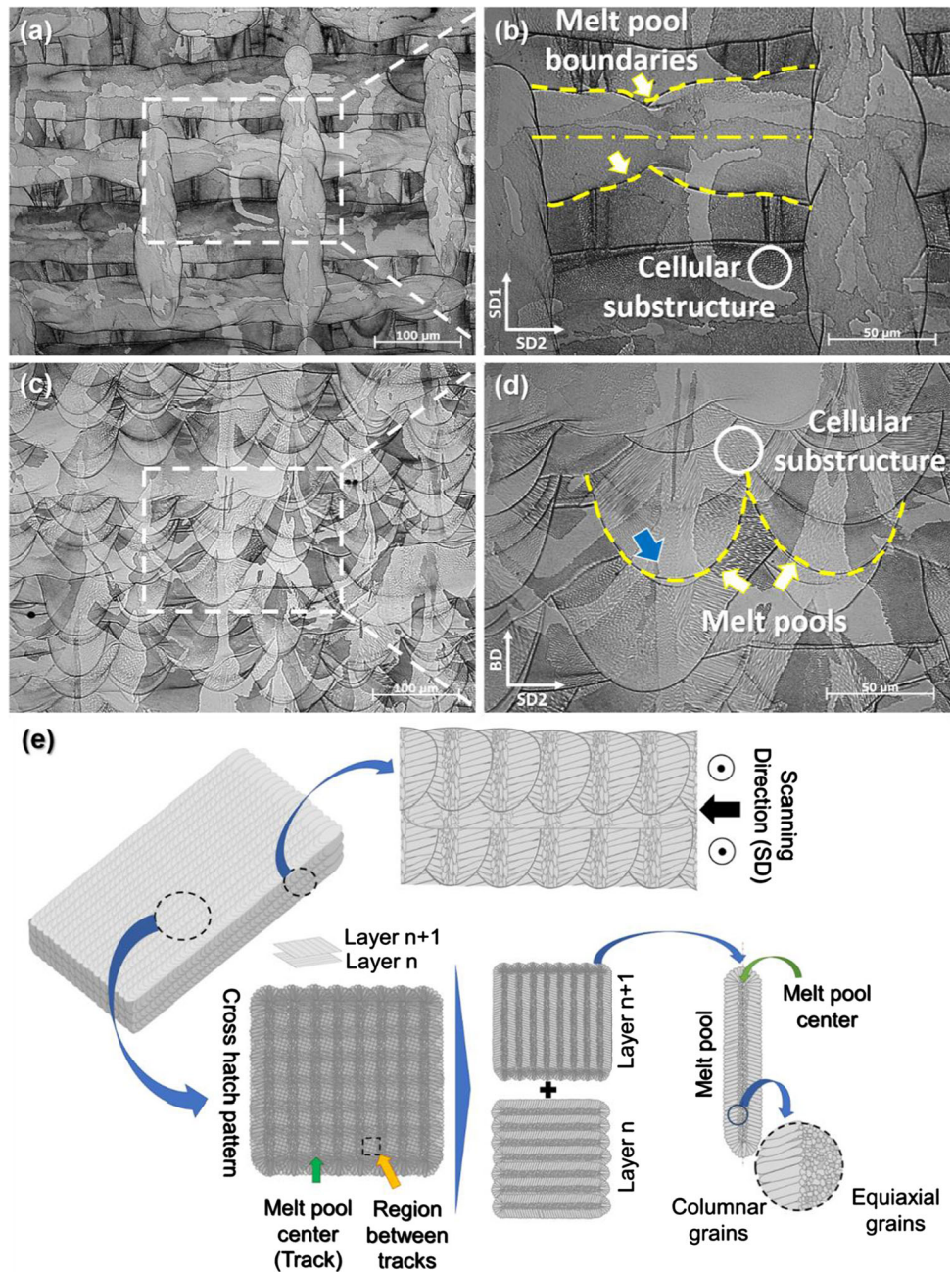
Coarser columnar grains grow inward from the sides of the melt pool, while finer columnar grains grow vertically in the melt pool center via epitaxial growth, due to the thermal gradient direction [40]. These square-shaped coarse-grained regions lying in between the path of the laser tracks are called “pockets” hereafter. The white circles in Fig. 3b and d highlight the presence of a cellular substructure.

Figure 4 shows an enlarged view of the microstructure.

Transmission electron microscopy studies showed that these dislocation cells have typical misorientations ranging from 0.5 to 1° in 316L stainless steel [10] and 0.2–0.8° in Hastelloy X [67] LPBF alloys. The formation of such solidification substructure is facilitated by ultra-high cooling rates that vary between  $10^3$  and  $10^6$  K/s [68, 69] together with high-temperature gradients (e.g., in the order of  $10^6$  K/m) [66]. The presence of a large number of nanoparticles dispersed in the matrix of this material is readily observed as indicated by the yellow arrows in Fig. 4. Fifteen ECCI-SEM images were used to calculate the average size of the cells and the particle size distribution in the as-built specimen. The average dislocation cell size found was  $383 \pm 40$  nm and the mean rhodonite-like particle size in this condition is  $37 \pm 19$  nm. The dislocation density of the as-built steel was estimated, according to the protocol described in Section “Annealing and microstructural characterization”, as being  $\sim 1.5 \times 10^{14} \text{ m}^{-2}$  (see Table 2). The literature reports that a rough estimate of  $\rho \sim 4 \times 10^{14} \text{ m}^{-2}$  can be assumed for LPBF materials having dislocation cells with sizes of  $\sim 400$  nm, which has a good agreement with our findings [70].

Figure 5a–c show the EBSD top view maps ( $\text{SD1} \times \text{SD2}$ ) of the sample, i.e., the maps were acquired from sections perpendicular to the build direction. Just as a pictorial remark, these engineered microstructures depicted as EBSD inverse pole figure (IPF) maps have geometric forms that very much resemble those found in some of the colorful paintings portrayed by F. Hundertwasser (1928–2000) and W. W. Kandinsky (1866–1944). The inverse pole figure (IPF) presented in Fig. 5a shows the grain orientations along the tracks and in the interior of the pockets. Small grains with sizes below 10  $\mu\text{m}$  are found in the tracks, whereas in the pockets they are much larger (50–60  $\mu\text{m}$ ). The difference in grain size between tracks and pockets is also observed in Fig. 3b, where fine grains are observed at the center of the laser tracks, while coarser square-shaped grains are observed between the laser tracks. The resulting chessboard pattern is created from the superposition of two perpendicular linear patterns (90° rotation), where epitaxial growth ensures the partial growth of grains from the previous layer onto the next one [45]. Figure 5b shows that high angle

**Figure 3** Microstructure of the as-built sample of AISI 316L stainless steel manufactured by LPBF (a, b) top view, (c, d) side view, as observed on an etched sample using light optical microscopy. The blue arrow shows an axially-oriented grain in the melt pool crossing several layers of the part (epitaxial growth) while the white circles mark a thin cellular structure which can be seen in both views of the part. (e) Schematic diagram depicting the microstructure resulting from the LPBF process using 90° rotation among layers. LPBF: laser powder-bed fusion.



boundaries (black lines) and low angle boundaries (red lines) are not evenly distributed in the microstructure. There is a much larger fraction of low angle boundaries along the laser tracks (about 0.35) and much less in the interior of the pockets (about 0.05). High angle boundaries respond for 0.6 of the total number of boundaries. From the side cross-section in Fig. 6a, one can observe that, although exhibited as equiaxed grains in the SD1 x SD2 cross-section, almost no equiaxed grains are visible in a 3D

perspective. Rather, grains are columnar and grow toward the BD.

KAM maps are useful to estimate the elastic stored energy in the material in a qualitative manner [71]. Low-misorientation dislocation cells like those depicted in Fig. 4 can be found throughout the microstructure (tracks and pockets); however, low angle boundaries with larger misorientations ( $2^{\circ}$ – $15^{\circ}$  interval) are more numerous along the tracks, leading to a local increase of stored energy (Fig. 5c).

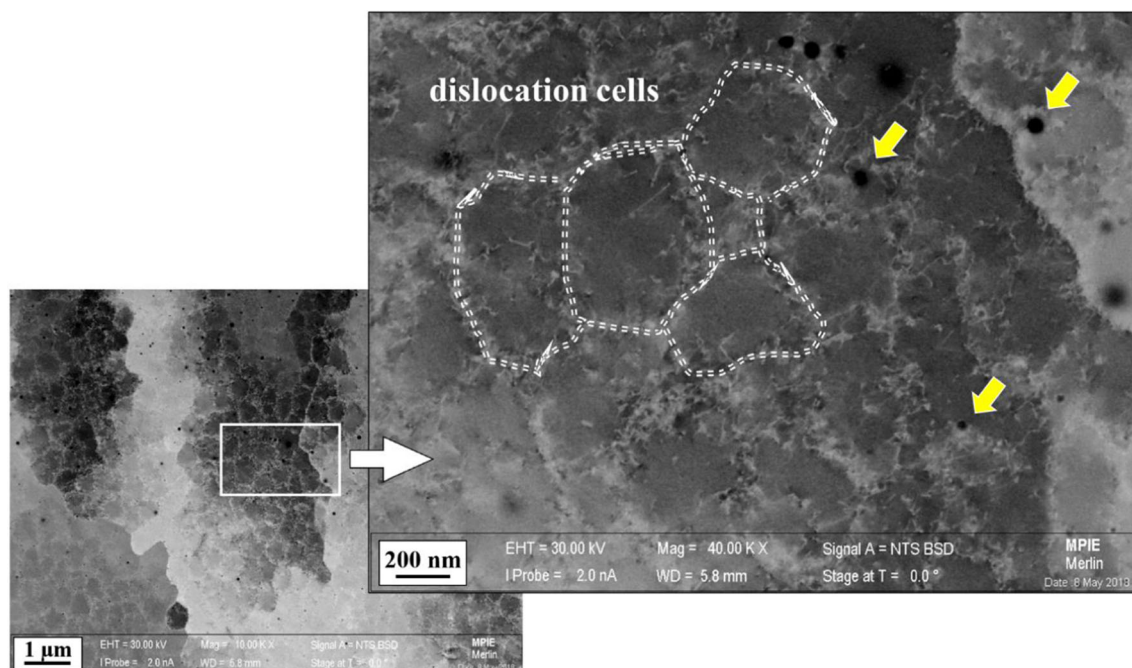


**Figure 4** Microstructure of the LPBF-processed 316L steel in the as-built condition using the electron channeling contrast imaging (ECCI) technique. Yellow arrows indicate spherical rhodonite-like nanoparticles.

**Table 2** Parameters obtained via both Rietveld-based refinement and Popa model for the as-built LPBF-processed AISI 316L steel.  $\langle D_{\text{eff}} \rangle$  and  $\langle \varepsilon_{\text{hh}}^2 \rangle^{1/2}$  are, respectively, the effective crystallite size and the accumulated microstrain.  $\rho$  stands for dislocation density. The goodness of fit (GoF) parameter is also displayed in this table

Condition	Lattice parameter (nm)	$\langle D_{\text{eff}} \rangle$ (nm)	Microstrain $\langle \varepsilon_{\text{hh}}^2 \rangle^{1/2}$	$\rho$ (m <sup>-2</sup> )	GoF
as-built	0.35899	190	0.00100	$1.5 \times 10^{14}$	1.38

Regions with locally fairly low dislocation densities inside of heterogeneously deformed microstructures can also provide regions that may act as potential recrystallization nuclei. This means that such nuclei may appear both, at low or at high dislocation density regions, depending on several factors such as the processing parameters, the studied material, and the degree of heterogeneity of the deformation substructure [72]. In all cases, such nuclei must be surrounded by at least one segment of a mobile high angle boundary [72, 73], where the adjacent deformed microstructure provides a higher stored elastic energy to drive the reaction in a net direction and sustain their growth. Therefore, it is important to identify, investigate and classify the nucleation sites, their spatial distribution, and their adjacent deformation substructure. A visualization of the possible recrystallization nucleation sites in a large section of

the LPBF-manufactured steel is given in Fig. 6. The former melt pool zones can be clearly recognized, and only high angle boundaries are indicated by black lines (Fig. 6c).

When applying the  $\text{GOS} \leq 1^\circ$  criterion, i.e., marking grains with high inner local crystalline perfection and negligible lattice curvature, possible recrystallization nucleation sites can be distinguished (Fig. 6b). However, a careful evaluation must be conducted when identifying recrystallized grains based solely on the GOS criterion, as smaller grains are known to intrinsically exhibit lower orientation spread values [73]. It must be stated that such grains are not recrystallized, as they have dislocation cells, although with a likely lower dislocation density. These local regions with lower dislocation density, yet surrounded by mobile high angle boundaries, possess the required conditions to serve as

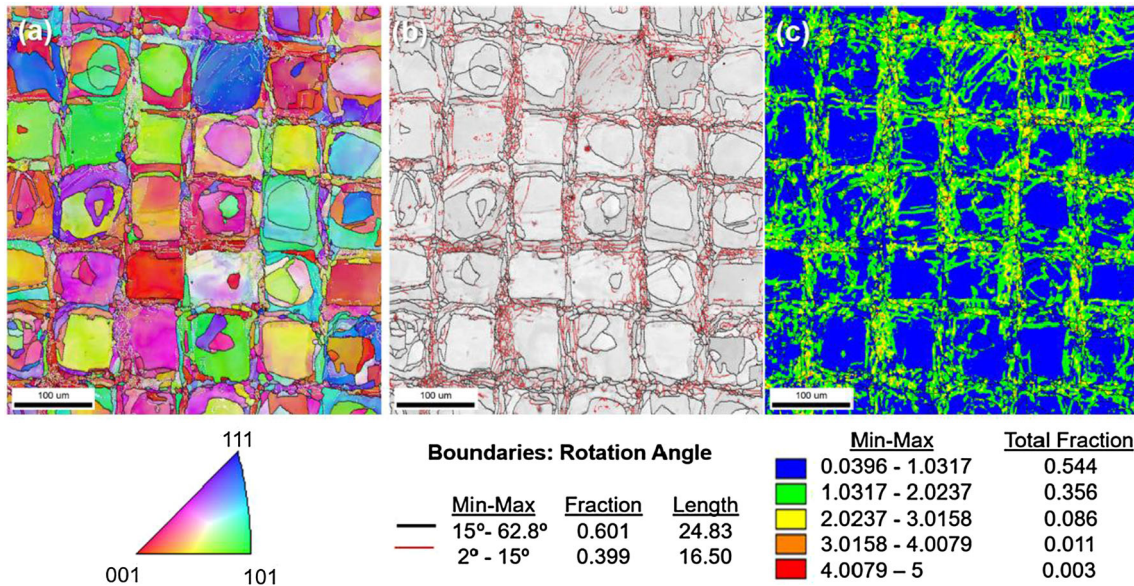
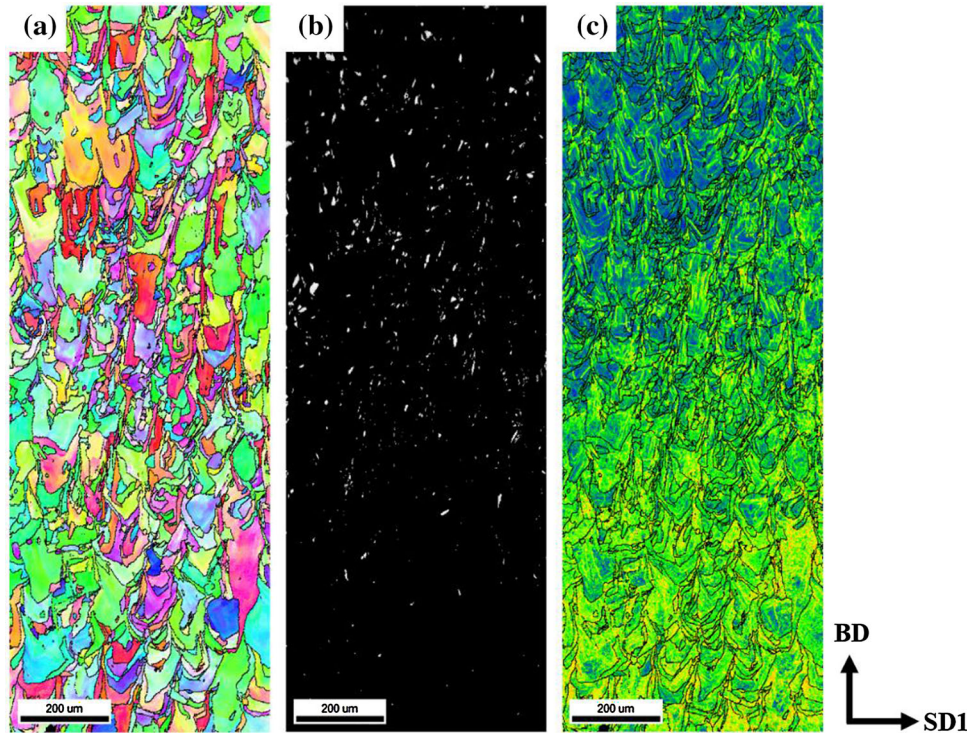


**Figure 5** EBSD maps of the build plane (SD1 x SD2) of AISI 316L steel manufactured by LPBF process in the as-built condition showing: **a** Inverse pole figure, **b** Image quality map indicating high angle boundaries marked by black lines and low angle

boundaries in red; **c** KAM maps of the corresponding IPF map. EBSD: electron backscatter diffraction; LPBF: laser powder-bed fusion; KAM: kernel average misorientation; IPF: inverse pole figure.

**Figure 6** EBSD maps of LPBF 316L steel in the as-built condition in the view parallel to the build direction showing: **a** IPF of the entire mapped area; **b** GOS map for regions displaying  $GOS \leq 1^\circ$ , constructed to highlight microstructure sites that could act as possible recrystallization nuclei; **c** KAM maps of the corresponding IPF map. LPBF: laser powder-bed fusion; IPF: inverse pole figure; GOS: grain orientation spread; KAM: kernel average misorientation; BD: building direction; SD1: scanning direction 1.



suitable nucleation sites upon annealing. Most of these nuclei are fairly elongated towards the build direction. Their spatial distribution is also non-uniform throughout the microstructure. This fact is related to the different levels of straining in the

microstructure (misorientation gradients) from the bottom to the top, as revealed by the KAM map shown in Fig. 6c. This difference in straining along BD may occur due to the variation of process conditions during building.

## Annealing behavior of as-built samples

Samples were annealed at 1150 °C for several time intervals. Based on the thermodynamic simulations displayed in Fig. 2a and on previous experiments (data not shown), this annealing temperature was chosen because only austenite and spinel ( $\text{MnCr}_2\text{O}_4$ ) should be present in the microstructure in equilibrium. Lower temperatures would make the progress of recrystallization sluggish, as the grain boundary mobility follows an Arrhenius-type thermal activation behavior, whereas higher temperatures would allow fast particle coarsening (see Section “Annealing behavior of as-built samples”), grain growth, or the likely formation of  $\delta$ -ferrite.

Figure 7a–d show the IPF maps of as-built and annealed samples at 1150 °C for 5, 15, and 60 min, respectively. Significant microstructural changes become noticeable only after 60 min of annealing. The initial chessboard-like pattern is replaced to some extent by a new microstructure, formed by equiaxed grains and annealing twins, as recrystallization progresses. After this period of time, only a small portion of the heat-treated microstructure preserves the initial features of the as-built condition.

The evolution of recrystallization and the identification of potential nucleation sites were investigated by constructing GOS maps from the EBSD data, as depicted in Fig. 8a–d. In these figures, the

recrystallized grains and possible recrystallization nuclei were considered as those with  $\text{GOS} \leq 1^\circ$  [74–76] and are displayed in white along their volume percentage. We distinguish possible recrystallization nuclei and recrystallized grains based on the presence of annealing twins, as both exhibit  $\text{GOS} \leq 1^\circ$ . The former is present up to 5 min annealing at 1150 °C, but such grains do not exhibit annealing twins nor morphology of recrystallized grains, differently from the recrystallized grains observed at 15 min annealing (1150 °C) onwards. Enlarged views of the samples depicted in Fig. 8b and c were chosen to highlight the nucleation sites, as reproduced in Fig. 9a–d. These results clearly indicate that nucleation occurs along the laser beam tracks (Fig. 9c). These regions hold the higher local stored energy and larger misorientations (Figs. 5 and 6) and the possible recrystallization nuclei (Fig. 6b). For the same reasons, at longer annealing times, the recrystallization front progresses along the tracks (higher stored energy) and then into the pockets (Fig. 9c and d) driven by the stored energy from dislocation cells and LABs formed due to static recovery.

According to the Johnson–Mehl–Avrami–Kolmogorov (JMAK) model [72], the volume fraction of recrystallized grains ( $X_v$ ) varies with time according to Eq. 2, where  $B$  is a constant and  $n$  is the Avrami exponent. This exponent depends on the material (stacking fault energy), dimensionality, and

**Figure 7** Inverse pole figures corresponding to the build plane (SD1 X SD2) of AISI 316L steel samples showing their recrystallization behavior at 1150 °C in the following conditions: **a** as-built; **b** 5 min, **c** 15 min, **d** 60 min. SD1 and SD2: scanning direction 1 and 2, respectively.

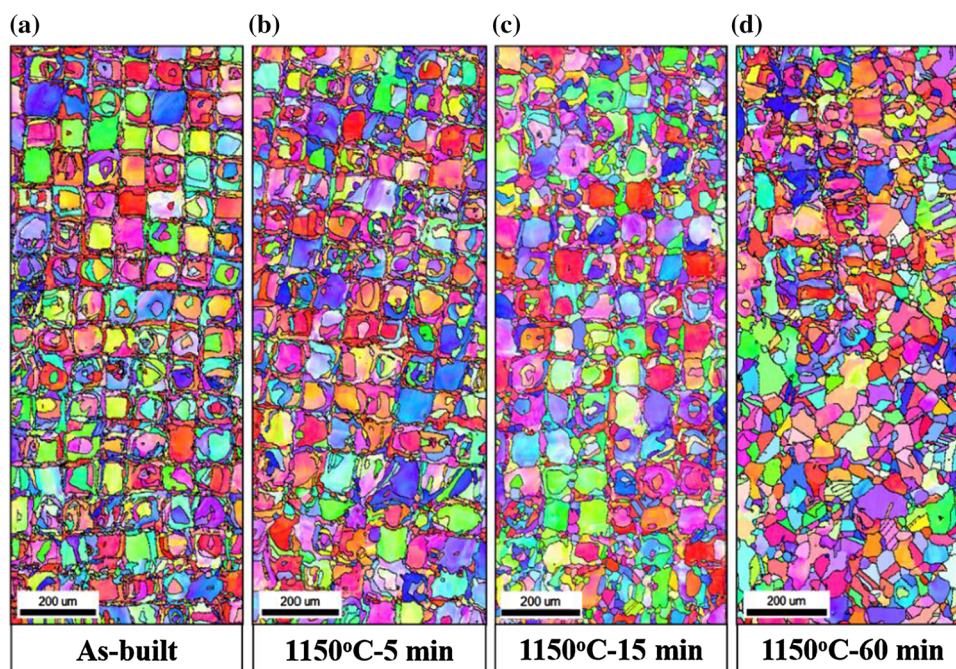
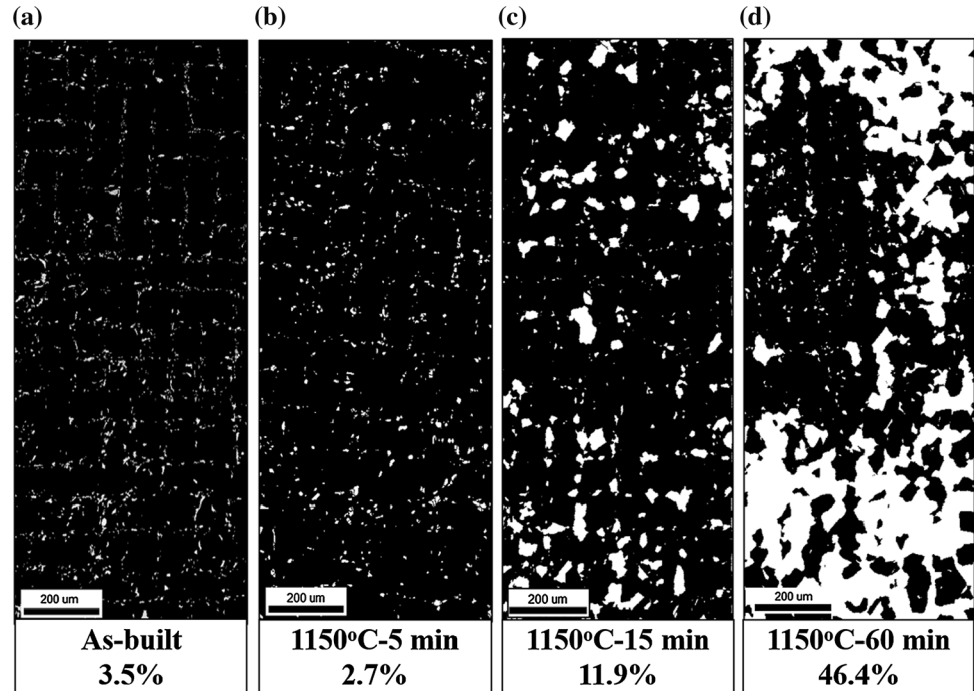


**Figure 8** Grain orientation spread (GOS) maps corresponding to the build plane (SD1 x SD2) shown in Fig. 7 showing the evolution of primary recrystallization: **a** as-built; **b** 5 min, **c** 15 min and **d** 60 min annealing at 1150 °C. Only grains with  $GOS \leq 1^\circ$  are depicted in white color. The corresponding recrystallized volume percentages are also indicated.



nucleation process (site saturation or constant nucleation rate).

$$X_V = 1 - \exp(-Bt^n) \quad (2)$$

Taking into account the values of  $X_V$  obtained from the EBSD data, and using Eq. (2), a value of  $n = 1.16$  was found (Fig. 10). Assuming that nucleation sites are randomly distributed, that all of them are available at  $t = 0$  s (site-saturation) and that isotropic growth occurs, the Avrami coefficient is expected to be 3. Low  $n$  values result from a non-random nucleation of recrystallization [72]. Compared to 304L grade, 316L stainless steel is less prone to undergo static recovery due to the high thermal stability resulting from Mo segregation at cell walls [21] and low-to-medium stacking fault energy of 33 mJ/m<sup>2</sup> [77]. Therefore, the low Avrami exponent of  $n = 1.16$ , herein observed, can be explained by the preferential nucleation and growth along the build tracks, restraining their growth along the transverse/building direction, as the build tracks exhibit higher dislocation density and higher local misorientation [45]. As a result, elongated recrystallized grains are observed in Fig. 9d. The most equiaxed grains are found at the pockets' corners, or at the regions where two perpendicular laser tracks meet. This occurs due to the fact that they are allowed to grow in 3D by consuming the build tracks along all directions.

The softening behavior and the corresponding JMAK plot are shown in Fig. 10. The hardness of the as-built specimen is  $246 \pm 10$  HV-0.2. Similar values were also reported in refs. [14, 69, 78]. These values are considerably higher than the ones found in wrought 316L stainless steel, namely, about 165 HV [69]. This difference is consistent with the complex dislocation cell structure observed in the present specimens and the presence of nanoparticles dispersed in the matrix [14]. The results also show that most of the softening occur during the first 240 min. For longer annealing times, the hardness levels out indicating that recrystallization is completed at less than 4 h at this temperature. Compared to our preceding work [45], where the recrystallization kinetics did not follow the JMAK behavior, the present study exhibits faster recrystallization kinetics (incomplete recrystallization after annealing at 1150 °C for 8 h in our previous study). The likely reason for such differences is the higher number density of recrystallized grains in the present study.

The discontinuous character of recrystallization is confirmed by clear nucleation and growth processes (Figs. 7 and 9). Contrastingly, continuous recrystallization does not exhibit such recognizable and consecutive steps (nucleation and growth) and is usually observed in highly strained materials, mainly at high annealing temperatures, where an increased fraction

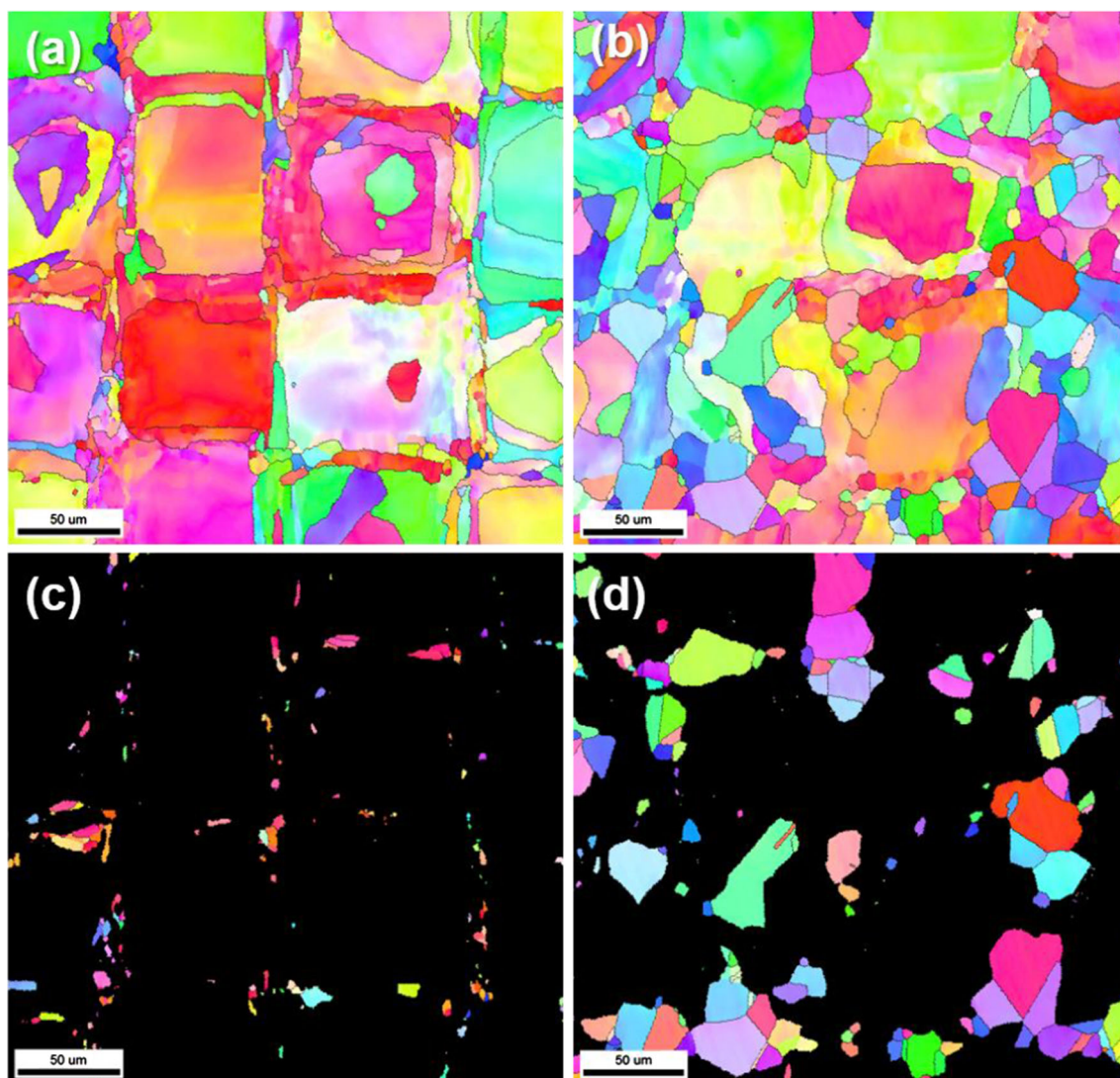


**Figure 9** Inverse pole figures depicting the build plane (top view – SD1 x SD2) of AISI 316L steel samples showing the nucleation of primary recrystallization at 1150 °C for: **a** 5 min and **b** 15 min.

Only grains with  $GOS \leq 1^\circ$  are depicted in the IPFs (c) and (d) for 5 and 15 min, respectively.

of high angle boundaries are present [72]. Upon annealing, the microstructure slightly changes in continuous recrystallization, frequently resulting in a fine-grained material. Such behavior is completely different from the response observed upon annealing for the current AISI 316L steel.

The population evolution of  $\Sigma 3$ -type boundaries (annealing twins), high angle (HAB), and low angle boundaries (LAB) is shown in Fig. 11. During primary recrystallization, the number of LABs decreases as the fraction of HABs steadily increases.  $\Sigma 3$ -type special boundaries (twins) are absent in the as-built condition. Only after 15 min, larger fractions of twins become noticeable in the microstructure, as depicted

in Fig. 9c, d and Fig. 11. Although the line fraction of annealing twins evidenced is relatively large (about 48%), it did not vary in a significant manner between 240 and 2880 min. This fraction of  $\Sigma 3$  boundaries after long-term annealing is significantly lower than the one reported for a grain-boundary engineered 316L stainless steel [79], where a fraction of 79% was present after 5% thickness reduction and annealing at 1027 °C for 30 min. It is known that grain-boundary-engineered alloys are subjected to low cold deformation (usually around 5% strain) followed by high-temperature annealing. In our alloy, the dislocation density is similar to a 20% tensile strained wrought-processed counterpart, which explains the reduced

**Figure 10** Softening behavior and JMAK plot (at the inset) of AISI 316L austenitic stainless steel produced by LPBF and annealed at 1150°C for several annealing times.  $X_v$ : recrystallized fraction;  $n$ : Avrami exponent;  $R$ : correlation coefficient.

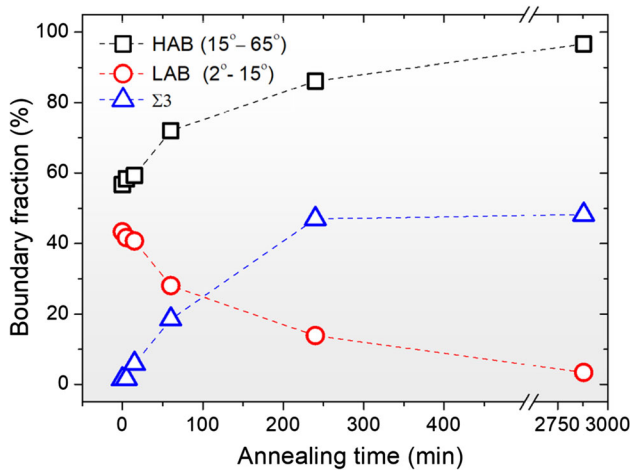
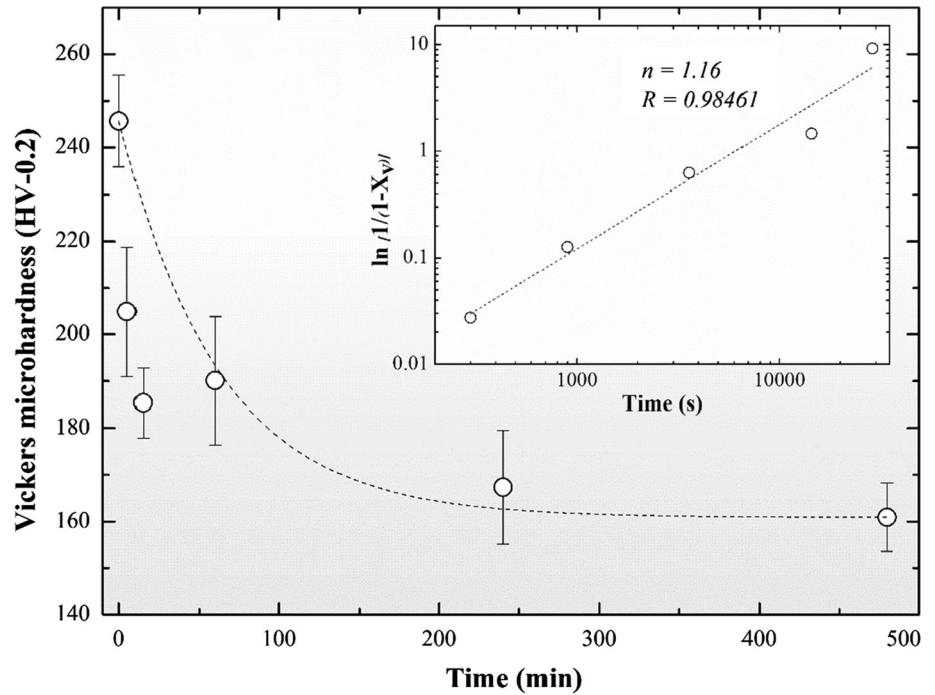


**Figure 11** Evolution of the length fraction of CSL— $\Sigma 3$ , high angle boundaries (HAB) and low angle boundaries (LAB) after isothermal annealing for various durations.

$\Sigma 3$  boundary fraction after annealing [80]. Thus, the  $\Sigma 3$  boundary fraction may be increased by controlled post-thermomechanical processing [44, 81].

### Driving and dragging pressures in recrystallization

The driving pressure for static recrystallization ( $P_D$ ) can be approximated by using Eq. 3 [82]:

$$P_D \approx 0.5\rho Gb^2 \tag{3}$$

where  $\rho$  is the dislocation density ( $1.5 \times 10^{14} \text{ m}^{-2}$ ), here obtained from Table 2,  $G$  is the shear modulus and  $b$  is the magnitude of the Burgers vector. Assuming  $b = 0.2541 \text{ nm}$  for austenite and  $G = 77 \text{ GPa}$  [83], the driving pressure for recrystallization in the as-built material (Eq. 2) can be calculated as  $3.7 \times 10^5 \text{ J/m}^3$  or  $0.37 \text{ MPa}$ . The drag force due to Zener-Smith pinning ( $P_z$ ) for the same initial condition can be estimated using Eq. 4 [84, 85]:

$$P_z = -3f\gamma_{GB}/2r \tag{4}$$

where  $f$  is the particle volume fraction,  $\gamma_{GB}$  is the grain boundary energy, and  $r$  is the particle radius. Taking a mean particle size  $2r = 37 \pm 19 \text{ nm}$ ,  $f = 0.25 \pm 0.11\%$ , and  $\gamma_{gb} = 668 \text{ mJ/m}^2$  [86], the calculated pinning pressure in the as-built condition is approximately  $6.8 \text{ MPa}$ . This number drops to  $0.9 \text{ MPa}$  when considering the particle size after 1-h annealing at  $1150^\circ\text{C}$  (viz.  $170 \pm 137 \text{ nm}$ ). These general estimates assume that both driving pressure (stored energy) and drag forces (particle distribution) are uniformly distributed in the microstructure. However, as the microstructure mapping revealed, this is not the present case. In qualitative terms, the stored energy was observed to be much larger along the building tracks. A rough estimate based on the

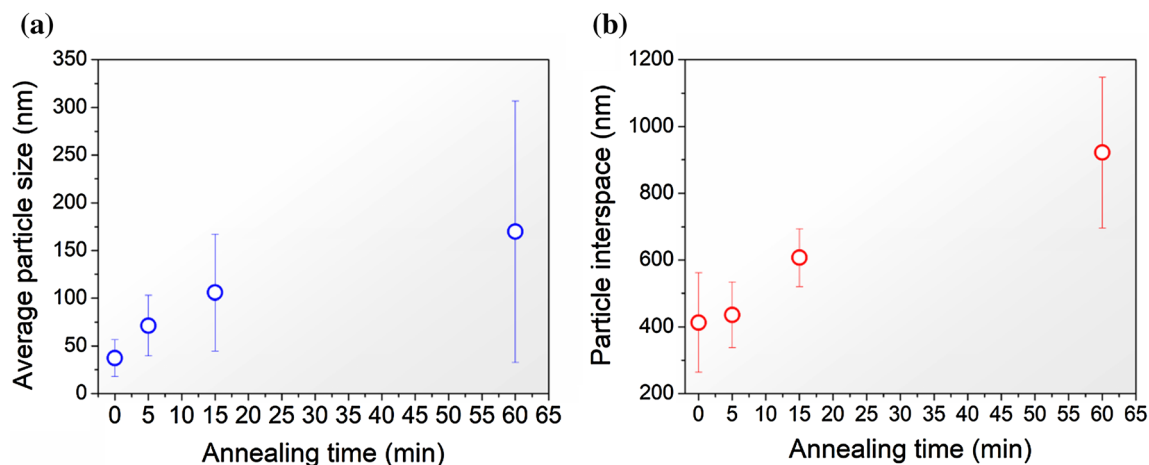


**Figure 12** Particle size evolution of nanoparticles in isothermally annealed samples at 1150°C: **a** mean particle size, **b** mean particle interspace.

misorientation distribution data from EBSD maps shows that about 40% of the total length of boundaries have low-angle character ( $2^{\circ}$ – $15^{\circ}$ ) (Figs. 5 and 11). In turn, these LABs are formed by geometrically necessary dislocations (GNDs). Since over 90% of the LABs are located along the melt tracks and about less than 10% are found within the pockets, the dislocation density and, thus, the stored energy for recrystallization is much larger in these regions, Fig. 9. Furthermore, nanoparticles are not evenly dispersed in the matrix making boundary pinning uneven in the microstructure.

### Particle-boundary interaction

As recrystallization proceeds, nanoparticles interact with high angle grain boundaries making their migration sluggish. The interaction between moving boundaries and particles enables a fast coarsening of the latter, which increases particle interspacing and causes a progressive decrease of the Zener-Smith pinning force (Eq. 4), as demonstrated in Fig. 12a, b. It is worth mentioning that these parameters (particle size and interspacing) are mean values taken from the global microstructure as a function of the annealing time.

To demonstrate that the interaction between high angle boundaries and particles speeds up Ostwald ripening, we measured the particle sizes in different regions (recrystallized grain interior, recrystallization front, and non-recrystallized grains). Figure 13a–c show SEM images depicting the evolution of the particle size with the progress of recrystallization. In

Fig. 13a, Ostwald ripening [87] of nanoparticles lying at the grain boundaries of the recrystallized grains is nearly twice as large as those in non-recrystallized regions after 5-min annealing. In general, particles coarsen, but the coarsening kinetics at grain boundaries or within recrystallized grains is faster than in recovered regions (Fig. 13b–d).

This difference in terms of particle coarsening kinetics can be mostly attributed to the much higher grain boundary diffusivity ( $D_b$ ) compared to the bulk one ( $D$ ). Determining  $D_b$  is a very complex experimental task and far from the scope of this work, since it depends on the local boundary width ( $\delta$ ) and on the boundary misorientation. Assuming  $\delta \approx 0.5$  nm, one can estimate that  $D_b$  is about four to eight orders of magnitude higher than  $D$ . Solute elements possessing high solubility in austenite speed up Ostwald ripening [88]. Thermokinetics calculations allowed to determine the diffusion coefficients and the solubility in austenite of five solute elements (Mn, Si, O, Cr, and Mo) over a wide range of temperature (900–1200 °C). For the sake of simplicity, we only focus on the bulk diffusivity of these species. This is justified because even in non-recrystallized regions, where bulk diffusivity is active, significant particle coarsening occurs. Figure 14a shows the changes of  $D$  as a function of temperature for several alloying elements in the austenite. Oxygen is an interstitial solute in austenite and it is the fastest-diffusing species among these five elements followed by Si, Mo, Mn, and Cr, in this order. Its bulk diffusivity is about 4 orders of magnitude higher than the other species at 1150 °C.

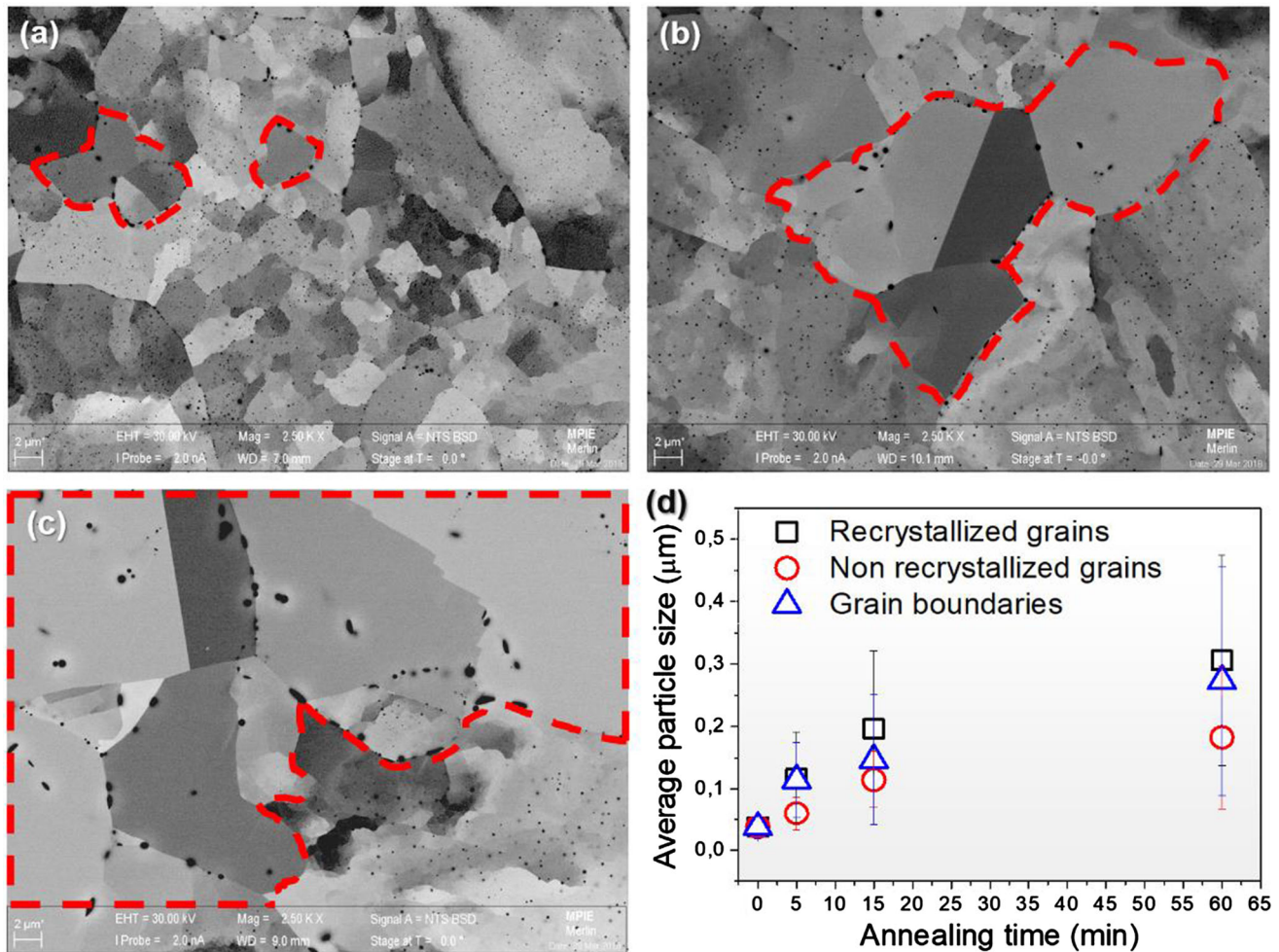


**Figure 13** ECCI images of the microstructure of AISI 316L steel annealed at 1150 °C showing the growth of nanoparticles with annealing time: (a) 5 min, (b) 15 min, and (c) 60 min.

These numbers support the experimental results concerning particle coarsening in this metal system.

Particle coarsening can be controlled by either bulk or grain boundary diffusion. According to Kirchner [89], the particle radius is proportional to  $t^{1/4}$  for particles sitting at the (high-angle) grain boundaries. For low-angle grain boundaries (subgrains), where pipe diffusion is the rate-controlling transport mechanism, the dependence drops to  $t^{1/5}$ . Taking the experimental points depicted in Fig. 12a, our data fit the dependence on  $t^{1/4}$ , in good agreement with the microstructural observations, i.e., enhanced particle coarsening due to grain boundary diffusion. One straight implication of particle coarsening is the change in corrosion properties upon annealing. An improvement of corrosion properties is observed due to the formation of a thicker and more

Recrystallized grains are surrounded by red dashed lines. The evolution of the particle size in each of these regions with time is shown in (d).

stable protective layer after annealing between 800 and 1050 °C [36, 90]. Contrastingly, a more negative corrosion potential is observed after annealing at 1200 °C up to 2 h, while a lower pitting potential was observed [26]. The reason is the formation of a less effective passivation film due to the presence of larger pores [26], likely created by the dissolution of particles during Ostwald ripening.

### Texture evolution

The crystallographic texture of LPBF materials depends on the heat flow and local nucleation conditions [91] and it can be tailored by adjusting the main process parameters, such as the laser beam power, the adopted scanning strategy, and the temperature of the build plate [92]. Figure 15a–e show

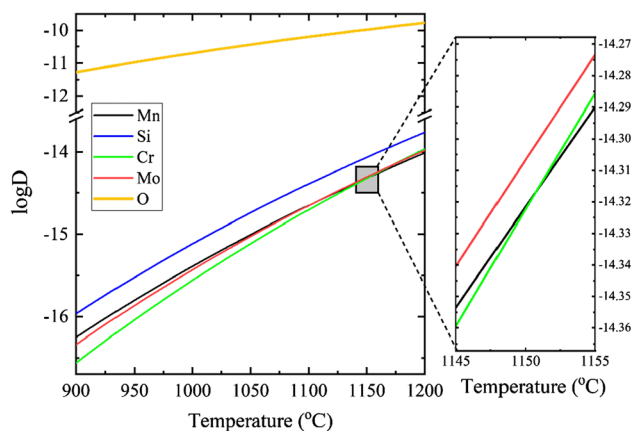


**Figure 14** Bulk diffusion coefficient ( $\text{m}^2/\text{s}$ ) of several solute elements (Mn, Si, O, Cr, and Mo) in the austenite within the temperature interval 900–1200 °C. This plot was calculated from Thermo-Calc software simulations and consider the global chemical composition of austenite. An enlarged view of the marked rectangle is shown on the right-hand side of this figure.

the contoured pole figures calculated from the EBSD mapping of the as-built condition and after annealing at 1150 °C for 5, 15, and 60 min, respectively. The scale bars are shown on the right-hand side of the pole figures for each condition. The texture intensity is expressed in terms of multiples of a random distribution (mrd). The material in the as-built condition has a weak texture (2.292 mrd) related to the Goss  $\{011\} \langle 001 \rangle$  component. When either possible recrystallization nuclei or recrystallized grains ( $\text{GOS} \leq 1^\circ$ ) are considered, their starting texture is also rather weak, as shown in Fig. 15e. As annealing proceeds, texture becomes random for practical purposes. The weak-to-absent texture in the as-built condition can be attributed to the low laser power (90 W) used in the manufacturing process of our samples [83], which favors nucleation of finer grains rather than strong epitaxial growth.

The laser power is the main processing parameter controlling the texture in LPBF alloys, as high laser powers lead to strong Goss  $\{110\} \langle 100 \rangle$  {BD}  $\langle \text{SD} \rangle$  textures [40, 45] or even single crystal-like parts [41]. Additionally, the scanning strategy plays a key role, as the rotation between layers weakens epitaxial growth, triggering nucleation of grains with different crystallographic orientations [93] and, thus, giving rise to overall weaker crystallographic textures. Upon annealing, the recrystallization weakens the texture further through the nucleation of strain-free grains, where twinning aids in creating a higher

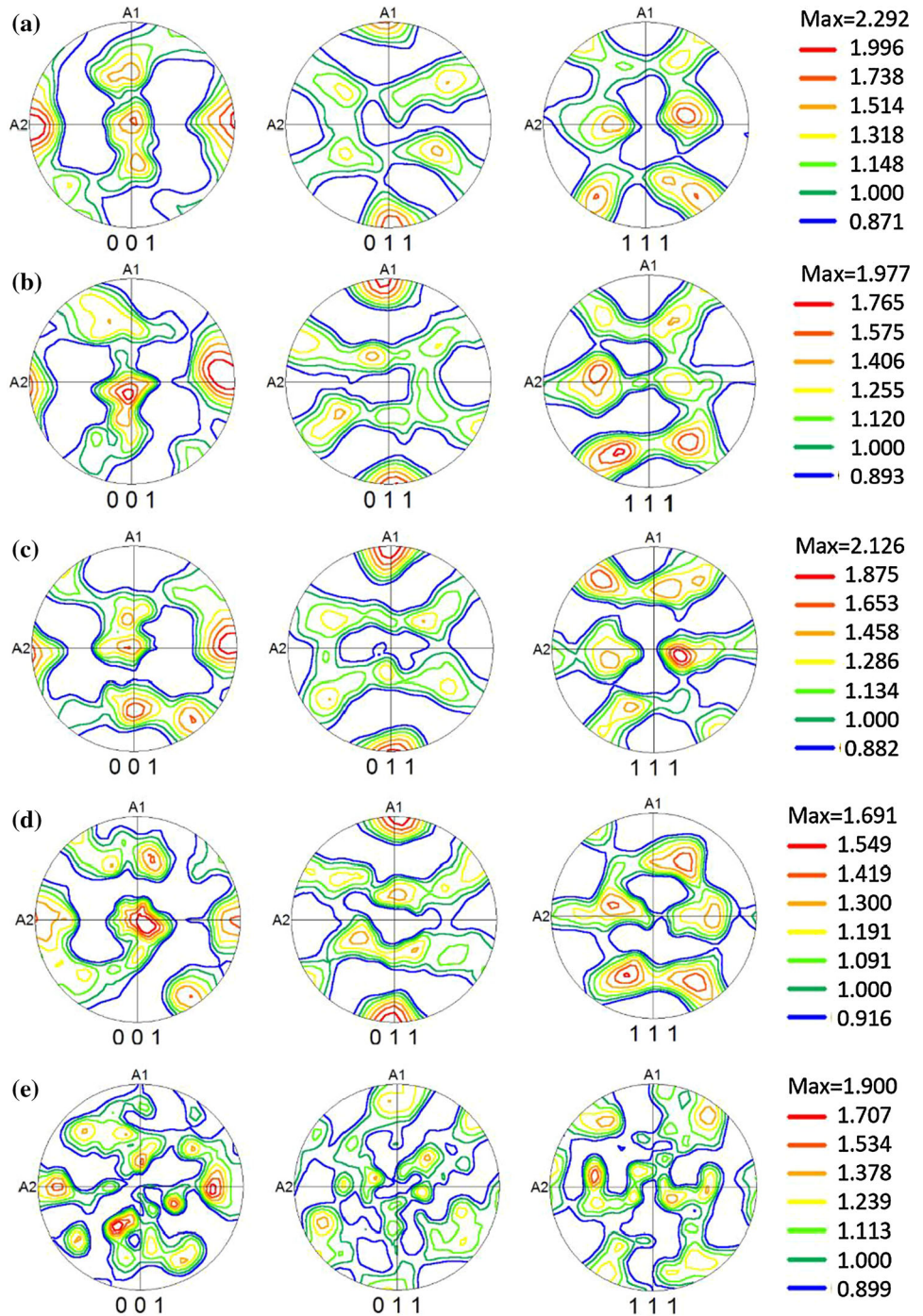
orientation variety of the crystallographic variants [94]. Texture strengthening occurs upon annealing only when abnormal grain growth occurs, where a few grains have a growth advantage and overgrow the matrix grains [95], which is not the behavior observed in this study. As a result, the weak texture of the as-built samples is randomized upon annealing. Texture intensities between as-built and annealed LPBF alloys are directly related. A similar AISI 316L with stronger texture (11.402 mrd vs. 2.292 mrd for the present as-built sample) in the as-built condition exhibits stronger texture after annealing at 1150 °C for 1 h (3.171 mrd) [45] when compared to the annealed samples in the present investigation (1.9 mrd). These results indicate that using the island scan strategy (with rotation between layers) combined with a low laser power followed by post-build recrystallization annealing gives rise to fairly isotropic texture and microstructures.

### Comparison of recrystallization kinetics between LPBF and conventionally manufactured materials

A straightforward comparison between the recrystallization kinetics of LPBF- and wrought-processed 316L stainless steel is not simple. Many microstructural parameters differ from one route to another depending on the processing conditions and might impact the recrystallization kinetics, such as starting grain size, texture, residual amounts of delta ferrite, strain-induced martensite (SIM) formation, chemical segregation, and so on. However, a general trend is observed when considering all the differences: the temperature to initiate the recrystallization in LPBF 316L is higher and the kinetics is more sluggish compared to the wrought manufactured counterpart. For example, recrystallization takes place at 700 °C for 1 h following 95% cold rolling reduction [94]. Complete recrystallization after 1000 °C for 30 min following 13% cold drawing is observed in another study [96]. For the steel herein investigated, incomplete recrystallization persists after annealing at 1150 °C for 4 h.

Considering all the microstructural features in wrought and LPBF 316L stainless steels, the weak texture and low strain found in the latter are apparently not the major contributors for the difference in their recrystallization kinetics, as seen in ref. [96]. Another point is the solute drag caused by

**Figure 15** Contoured pole figures calculated from the EBSD maps: (a) as-built; (b–d) isothermally annealed samples at 1150 °C for 5, 15, and 60 min, respectively. Only grains with GOS  $\leq 1^\circ$  (possible recrystallization nuclei or recrystallized grains) are counted in the PF (e) for the sample annealed at 1150 °C for 5 min. Texture intensities are shown on the right-hand side of the pole figures in terms of multiple of a random distribution (mrd). EBSD: electron backscatter diffraction; GOS: grain orientation spread; PF: pole figures; A1: building direction; A2: scanning direction.



molybdenum segregation at cell walls in the as-built LPBF AISI 316L, which guarantees enhanced thermal stability [21]. Despite this factor, molybdenum segregation was not investigated in detail, since the matrix is chemically homogenized before 10 s at the investigated temperature, as observed by thermokinetic simulations using the DICTRA software [45]. Therefore, our results suggest that, in LPBF-316L

stainless steel, recrystallization is mainly controlled by particle coarsening and heterogeneous nuclei distribution. Thus, LPBF alloys, which frequently contain a fine dispersion of nanoparticles, exhibit a sluggish recrystallization kinetics when compared to a wrought counterpart (for other alloys as well [46]) due to the interaction of nanoparticles with migrating grain boundaries.

Our study reports the in-depth characterization of the recrystallization kinetics and the importance of the as-built LPBF microstructure, especially nanoparticles, on this phenomenon. We quantitatively show that recrystallization is mainly controlled by particle coarsening with annealing and the concurrent decrease of the Zener-Smith pinning force. These results confirm that the yield stress and other mechanical properties can be tuned by controlling a given recrystallized volume fraction and their nucleation sites by a combination of proper process parameters (scanning strategy and laser beam power) and post-processing recrystallization annealing.

## Summary and conclusions

The post-build annealing behavior of texture-free AISI 316L austenitic stainless-steel cylinders manufactured by LPBF additive manufacturing was investigated at 1150 °C. The main microstructural changes upon annealing were followed by means of several characterization techniques such as strain analysis from EBSD data (GOS and KAM maps), XRD, and quantitative metallography. Based on the main findings reported in this work, the following conclusions can be drawn:

- (a) A larger fraction of low angle boundaries can be noticed along the melt tracks (center of the melt pools) compared to the pockets (sides of the melt pools). In the as-built condition, potential recrystallization nuclei lie fairly parallel to the build direction at the intersections of the melt tracks of layers  $n$  and  $n + 1$ , i.e., regions with higher stored elastic energy.
- (b) Recrystallization starts at the melt tracks because of their larger stored energy. Recrystallization proceeds along these tracks and after consuming them, migrate towards the coarse-grained areas (pockets).
- (c) Recrystallization kinetics is most affected by particle coarsening. The Zener-Smith pinning pressure exerted by nanoparticles progressively decreases upon annealing due to coarsening. When particles reach a critical size, the recrystallization front is released since the driving pressure overcomes the dragging one.
- (d) The interaction between the second-phase particles and the recrystallization front, where grain boundary diffusivity is the most active mass transport mechanism, allows fast Ostwald ripening. The mean particle size increases from  $37 \pm 19$  nm to  $170 \pm 137$  nm after 1-h annealing. Longer annealing times transform rhodnite ( $\text{MnSiO}_3$ ) into spinel-type manganese chromate ( $\text{MnCr}_2\text{O}_4$ ) particles, the predicted equilibrium phase.
- (e) The recrystallization kinetics is particularly sluggish due to the non-random distribution of nuclei, as suggested by the low value of the Avrami exponent  $n = 1.16$  and concurrent pinning effects.

## Acknowledgements

The authors are grateful to FAPESP (Sao Paulo Research Foundation, Brazil) for the financial support (Grant 2017/02485-2). LSA also acknowledges São Paulo Research Foundation (FAPESP) FAPESP for his scholarship (Grants 2018/23582-9 and 2019/19442-0). HRZS is CNPq Fellow (The National Council for Scientific and Technological Development, Brazil) under Grant 302.136/2017-7. IRSF acknowledges financial support through CAPES-Humboldt (Grant 88881.512949/2020-01). Dr. Jorge Vicente da Silva and BSc. Paulo Inforçatti (CTI Renato Archer, Campinas, Brazil) is gratefully acknowledged for processing the LPBF parts for this investigation.

## Funding

Open Access funding enabled and organized by Projekt DEAL.

## Declarations

**Conflict of interest** The authors declare that no conflict of interests or competing interests exists that could have influenced the work reported in the paper.

**Open Access** This article is licensed under a Creative Commons Attribution 4.0 International License, which permits use, sharing, adaptation, distribution and reproduction in any medium or format, as long as you give appropriate credit to the original author(s) and the source, provide a link to the

Creative Commons licence, and indicate if changes were made. The images or other third party material in this article are included in the article's Creative Commons licence, unless indicated otherwise in a credit line to the material. If material is not included in the article's Creative Commons licence and your intended use is not permitted by statutory regulation or exceeds the permitted use, you will need to obtain permission directly from the copyright holder. To view a copy of this licence, visit <http://creativecommons.org/licenses/by/4.0/>.

## References

- [1] Gu DD, Meiners W, Wissenbach K, Poprawe R (2012) Laser additive manufacturing of metallic components: materials, processes and mechanisms. *Int Mater Rev* 57:133–164. <https://doi.org/10.1179/1743280411Y.0000000014>
- [2] Frazier WE (2014) Metal additive manufacturing: a review. *J Mater Eng Perform* 23:1917–1928. <https://doi.org/10.1007/s11665-014-0958-z>
- [3] Sames WJ, List FA, Pannala S, Dehoff RR, Babu SS (2016) The metallurgy and processing science of metal additive manufacturing. *Int Mater Rev* 61:315–360. <https://doi.org/10.1080/09506608.2015.1116649>
- [4] Niendorf T, Leuders S, Riemer A, Richard HA, Tröster T, Schwarze D (2013) Highly anisotropic steel processed by selective laser melting. *Metall Mater Trans B Process Metall Mater Process Sci* 44:794–796. <https://doi.org/10.1007/s11663-013-9875-z>
- [5] Thijs L, Montero Sistiaga ML, Wauthle R, Xie Q, Kruth JP, Van Humbeeck J (2013) Strong morphological and crystallographic texture and resulting yield strength anisotropy in selective laser melted tantalum. *Acta Mater* 61:4657–4668. <https://doi.org/10.1016/j.actamat.2013.04.036>
- [6] Carter LN, Martin C, Withers PJ, Attallah MM (2014) The influence of the laser scan strategy on grain structure and cracking behaviour in SLM powder-bed fabricated nickel superalloy. *J Alloys Compd* 615:338–347. <https://doi.org/10.1016/j.jallcom.2014.06.172>
- [7] Kok Y, Tan XP, Wang P, Nai MLS, Loh NH, Liu E, Tor SB (2018) Anisotropy and heterogeneity of microstructure and mechanical properties in metal additive manufacturing: a critical review. *Mater Des* 139:565–586. <https://doi.org/10.1016/j.matdes.2017.11.021>
- [8] Murr LE (2018) A metallographic review of 3D printing/additive manufacturing of metal and alloy products and components. *Metallogr Microstruct Anal* 7:103–132. <https://doi.org/10.1007/s13632-018-0433-6>
- [9] Bajaj P, Hariharan A, Kini A, Kürnsteiner P, Raabe D, Jägler EA (2020) Steels in additive manufacturing: a review of their microstructure and properties. *Mater Sci Eng A*. 772:1386–33. <https://doi.org/10.1016/j.msea.2019.138633>
- [10] Wang YM, Voisin T, McKeown JT, Ye J, Calta NP, Li Z, Zeng Z, Zhang Y, Chen W, Roehling TT, Ott RT, Santala MK, Depond PJ, Matthews MJ, Hamza AV, Zhu T (2017) Additively manufactured hierarchical stainless steels with high strength and ductility. *Nat Mater*. 17: 63–71. <https://doi.org/10.1038/nmat5021>
- [11] Lou X, Andresen PL, Rebak RB (2018) Oxide inclusions in laser additive manufactured stainless steel and their effects on impact toughness and stress corrosion cracking behavior. *J Nucl Mater* 499:182–190. <https://doi.org/10.1016/j.jnucmat.2017.11.036>
- [12] Tang M, Pistorius PC (2017) Oxides, porosity and fatigue performance of AlSi10Mg parts produced by selective laser melting. *Int J Fatigue* 94:192–201. <https://doi.org/10.1016/j.ijfatigue.2016.06.002>
- [13] Gasper AND, Hickman D, Ashcroft I, Sharma S, Wang X, Szost B, Johns D, Clare AT (2019) Oxide and spatter powder formation during laser powder bed fusion of Hastelloy X. *Powder Technol* 354:333–337. <https://doi.org/10.1016/j.powtec.2019.06.004>
- [14] Yan F, Xiong W, Faierson E, Olson GB (2018) Characterization of nano-scale oxides in austenitic stainless steel processed by powder bed fusion. *Scr Mater* 155:104–108. <https://doi.org/10.1016/j.scriptamat.2018.06.011>
- [15] Song B, Dong S, Liu Q, Liao H, Coddet C (2014) Vacuum heat treatment of iron parts produced by selective laser melting: microstructure, residual stress and tensile behavior. *Mater Des* 54:727–733. <https://doi.org/10.1016/j.matdes.2013.08.085>
- [16] Kanagarajah P, Brenne F, Niendorf T, Maier HJ (2013) Inconel 939 processed by selective laser melting: effect of microstructure and temperature on the mechanical properties under static and cyclic loading. *Mater Sci Eng A* 588:188–195. <https://doi.org/10.1016/j.msea.2013.09.025>
- [17] Hengsbach F, Koppa P, Duschik K, Holzweissig MJ, Burns M, Nellesen J, Tillmann W, Tröster T, Hoyer K-P, Schaper M (2017) Duplex stainless steel fabricated by selective laser melting - Microstructural and mechanical properties. *Mater Des* 133:136–142. <https://doi.org/10.1016/j.matdes.2017.07.046>
- [18] Suzuki H (1983) Weldability of modern structural steels in Japan. *Trans Iron Steel Inst Japan* 23:189–204. <https://doi.org/10.2355/isijinternational1966.23.189>
- [19] Liu F, Lin X, Yang G, Song M, Chen J, Huang W (2011) Microstructure and residual stress of laser rapid formed

- Inconel 718 nickel-base superalloy. *Opt Laser Technol* 43:208–213. <https://doi.org/10.1016/j.optlastec.2010.06.015>
- [20] Bertsch KM, Meric de Bellefon G, Kuehl B, Thoma DJ (2020) Origin of dislocation structures in an additively manufactured austenitic stainless steel 316L. *Acta Mater* 199:19–33. <https://doi.org/10.1016/j.actamat.2020.07.063>
- [21] Deng P, Yin H, Song M, Li D, Zheng Y, Prorok BC, Lou X (2020) On the thermal stability of dislocation cellular structures in additively manufactured austenitic stainless steels: roles of heavy element segregation and stacking fault energy. *Jom* 72:4232–4243. <https://doi.org/10.1007/s11837-020-04427-7>
- [22] Chen N, Ma G, Zhu W, Godfrey A, Shen Z, Wu G, Huang X (2019) Enhancement of an additive-manufactured austenitic stainless steel by post-manufacture heat-treatment. *Mater Sci Eng A* 759:65–69. <https://doi.org/10.1016/j.msea.2019.04.111>
- [23] Salman OO, Gammer C, Chaubey AK, Eckert J, Scudino S (2019) Effect of heat treatment on microstructure and mechanical properties of 316L steel synthesized by selective laser melting. *Mater Sci Eng A* 748:205–212. <https://doi.org/10.1016/j.msea.2019.01.110>
- [24] Sistiaga MLM, Nardone S, Hautfenne C, Van Humbeeck J (2016) Effect of heat treatment of 316L stainless steel produced by Selective Laser Melting (SLM). In: *Proceedings of the 27th Annual International Solid Freeform Fabrication Symposium-An Additive Manufacturing Conference. Solid Freeform Fabrication*, p 558–565, 8–10 July 2016
- [25] Lou X, Song M, Emigh PW, Othon MA, Andresen PL (2017) On the stress corrosion crack growth behaviour in high temperature water of 316L stainless steel made by laser powder bed fusion additive manufacturing. *Corros Sci* 128:140–153. <https://doi.org/10.1016/j.corsci.2017.09.017>
- [26] Kong D, Dong C, Ni X, Zhang L, Yao J, Man C, Cheng X, Xiao K, Li X (2019) Mechanical properties and corrosion behavior of selective laser melted 316L stainless steel after different heat treatment processes. *J Mater Sci Technol* 35:1499–1507. <https://doi.org/10.1016/j.jmst.2019.03.003>
- [27] Jiang R, Mostafaei A, Pauza J, Kantzos C, Rollett AD (2019) Varied heat treatments and properties of laser powder bed printed Inconel 718. *Mater Sci Eng A* 755:170–180. <https://doi.org/10.1016/j.msea.2019.03.103>
- [28] Davies SJ, Jeffs SP, Coleman MP, Lancaster RJ (2018) Effects of heat treatment on microstructure and creep properties of a laser powder bed fused nickel superalloy. *Mater Des* 159:39–46. <https://doi.org/10.1016/j.matdes.2018.08.039>
- [29] Yan F, Xiong W, Faierson EJ (2017) Grain structure control of additively manufactured metallic materials. *Materials (Basel)* 10:1260. <https://doi.org/10.3390/ma1011260>
- [30] Tian Z, Zhang C, Wang D, Liu W, Fang X, Wellmann D, Zhao Y, Tian Y (2020) A review on laser powder bed fusion of inconel 625 nickel-based alloy. *Appl Sci* 10:81. <https://doi.org/10.3390/app10010081>
- [31] Shamsujjoha M, Agnew SR, Fitz-Gerald JM, Moore WR, Newman TA (2018) High strength and ductility of additively manufactured 316L stainless steel explained. *Metall Mater Trans A Phys Metall Mater Sci* 49:3011–3027. <https://doi.org/10.1007/s11661-018-4607-2>
- [32] Fergani O, Bratli Wold A, Berto F, Brotan V, Bambach M (2018) Study of the effect of heat treatment on fatigue crack growth behaviour of 316L stainless steel produced by selective laser melting. *Fatigue Fract Eng Mater Struct* 41:1102–1119. <https://doi.org/10.1111/ffe.12755>
- [33] Kempen K, Thijs L, Van Humbeeck J, Kruth JP (2012) Mechanical properties of AlSi10Mg produced by selective laser melting. *Phys Procedia* 39:439–446. <https://doi.org/10.1016/j.phpro.2012.10.059>
- [34] Geenen K, Röttger A, Theisen W (2017) Corrosion behavior of 316L austenitic steel processed by selective laser melting, hot-isostatic pressing, and casting. *Mater Corros* 68:764–775. <https://doi.org/10.1002/maco.201609210>
- [35] Ventura AP, Wade CA, Pawlikowski G, Bayes M, Watanabe M, Misiolek WZ (2016) Mechanical properties and microstructural characterization of Cu-4.3 Pct Sn fabricated by selective laser melting. *Metall Mater Trans A Phys Metall Mater Sci* 48:1–10. <https://doi.org/10.1007/s11661-016-3779-x>
- [36] Kong D, Ni X, Dong C, Zhang L, Man C, Yao J, Xiao K, Li X (2018) Heat treatment effect on the microstructure and corrosion behavior of 316L stainless steel fabricated by selective laser melting for proton exchange membrane fuel cells. *Electrochim Acta* 276:293–303. <https://doi.org/10.1016/j.electacta.2018.04.188>
- [37] Fang XY, Li HQ, Wang M, Li C, Guo YB (2018) Characterization of texture and grain boundary character distributions of selective laser melted Inconel 625 alloy. *Mater Charact* 143:182–190. <https://doi.org/10.1016/j.matchar.2018.02.008>
- [38] Chlebus E, Gruber K, Kuźnicka B, Kurzac J, Kurzynowski T (2015) Effect of heat treatment on microstructure and mechanical properties of Inconel 718 processed by selective laser melting. *Mater Sci Eng A* 639:647–655. <https://doi.org/10.1016/j.msea.2015.05.035>
- [39] Bahl S, Mishra S, Yazar KU, Kola IR, Chatterjee K, Suwas S (2019) Non-equilibrium microstructure, crystallographic texture and morphological texture synergistically result in unusual mechanical properties of 3D printed 316L stainless steel. *Addit Manuf* 28:65–77. <https://doi.org/10.1016/j.addma.2019.04.016>

- [40] Sun SH, Ishimoto T, Hagihara K, Tsutsumi Y, Hanawa T, Nakano T (2019) Excellent mechanical and corrosion properties of austenitic stainless steel with a unique crystallographic lamellar microstructure via selective laser melting. *Scr Mater* 159:89–93. <https://doi.org/10.1016/j.scriptamat.2018.09.017>
- [41] Gokcekaya O, Ishimoto T, Hibino S, Yasutomi J, Narushima T, Nakano T (2021) Unique crystallographic texture formation in Inconel 718 by laser powder bed fusion and its effect on mechanical anisotropy. *Acta Mater.* 212:116876 <https://doi.org/10.1016/j.actamat.2021.116876>
- [42] Zeng Q, Gan K, Wang Y (2021) Effect of heat treatment on microstructures and mechanical behaviors of 316L stainless steels synthesized by selective laser melting. *J Mater Eng Perform* 30:409–422. <https://doi.org/10.1007/s11665-020-05330-7>
- [43] Waqar S, Liu J, Sun Q, Guo K, Sun J (2020) Effect of post-heat treatment cooling on microstructure and mechanical properties of selective laser melting manufactured austenitic 316L stainless steel. *Rapid Prototyp J* 26:1739–1749. <https://doi.org/10.1108/RPJ-12-2019-0320>
- [44] Gao S, Hu Z, Duchamp M, Krishnan PSSR, Tekumalla S, Song X, Seita M (2020) Recrystallization-based grain boundary engineering of 316L stainless steel produced via selective laser melting. *Acta Mater* 200:366–377. <https://doi.org/10.1016/j.actamat.2020.09.015>
- [45] Aota LS, Bajaj P, Zilnyk KD, Jäggle EA, Ponge D, Sandim HRZ, Raabe D (2021) Recrystallization kinetics, mechanisms, and topology in alloys processed by laser powder-bed fusion: AISI 316L stainless steel as example. *Materialia* 20:101236. <https://doi.org/10.1016/j.mtla.2021.101236>
- [46] Ariasetta A, Kobayashi S, Takeyama M, Wang Y, Imano S (2020) Characterization of recrystallization and second-phase particles in solution-treated additively manufactured alloy 718. *Metall Mater Trans A Phys Metall Mater Sci* 51:973–981. <https://doi.org/10.1007/s11661-019-05560-y>
- [47] Pinto FC, Filho IRS, Sandim MJR, Sandim HRZ (2020) Defects in parts manufactured by selective laser melting caused by  $\delta$ -ferrite in reused 316L steel powder feedstock. *Addit Manuf* 31:100979. <https://doi.org/10.1016/j.addma.2019.100979>
- [48] Lutterotti L, MAUD, version 2.038, (2006)
- [49] Lutterotti L, Scardi P (1990) Simultaneous structure and size-strain refinement by the Rietveld method. *J Appl Crystallogr* 23:246–252. <https://doi.org/10.1107/S0021889890002382>
- [50] Popa NC (1998) The (hkl) dependence of diffraction-line broadening caused by strain and size for all Laue groups in Rietveld refinement. *J Appl Crystallogr* 31:176–180. <https://doi.org/10.1107/S0021889897009795>
- [51.] Prince E (1993) The Rietveld method. Oxford University Press, Oxford, UK
- [52] Sahu P, De M, Kajiwara S (2002) Microstructural characterization of stress-induced martensites evolved at low temperature in deformed powders of Fe–Mn–C alloys by the Rietveld method. *J Alloys Compd* 346:158–169. [https://doi.org/10.1016/S0925-8388\(02\)00495-4](https://doi.org/10.1016/S0925-8388(02)00495-4)
- [53] Williamson GK, Smallman RE III (1956) Dislocation densities in some annealed and cold-worked metals from measurements on the X-ray Debye-Scherrer spectrum. *Philos Mag* 1:34–46. <https://doi.org/10.1080/14786435608238074>
- [54] Deng P, Karadge M, Rebak RB, Gupta VK, Prorok BC, Lou X (2020) The origin and formation of oxygen inclusions in austenitic stainless steels manufactured by laser powder bed fusion. *Addit Manuf* 35:101334. <https://doi.org/10.1016/j.addma.2020.101334>
- [55] Munitz A, Venkert A, Landau P, Kaufman MJ, Abbaschian R (2012) Microstructure and phase selection in supercooled copper alloys exhibiting metastable liquid miscibility gaps. *J Mater Sci* 47:7955–7970. <https://doi.org/10.1007/s10853-012-6354-x>
- [56] Saeidi K, Gao X, Zhong Y, Shen ZJ (2015) Hardened austenite steel with columnar sub-grain structure formed by laser melting. *Mater Sci Eng A* 625:221–229. <https://doi.org/10.1016/j.msea.2014.12.018>
- [57] Riabov D, Rashidi M, Hryha E, Bengtsson S (2020) Effect of the powder feedstock on the oxide dispersion strengthening of 316L stainless steel produced by laser powder bed fusion. *Mater Charact* 169:110582. <https://doi.org/10.1016/j.matchar.2020.110582>
- [58] Luo SB, Wang WL, Chang J, Xia ZC, Wei B (2014) A comparative study of dendritic growth within undercooled liquid pure Fe and Fe<sub>50</sub>Cu<sub>50</sub> alloy. *Acta Mater* 69:355–364. <https://doi.org/10.1016/j.actamat.2013.12.009>
- [59] Sun WP, Militzer M, Jonas JJ (1992) Diffusion-controlled growth and coarsening of MnS during hot deformation. *Metall Mater Trans A* 23A:3013–3023. <https://doi.org/10.1007/BF02646119>
- [60] Sun Z, Tan X, Tor SB, Yeong WY (2016) Selective laser melting of stainless steel 316L with low porosity and high build rates. *Mater Des* 104:197–204. <https://doi.org/10.1016/j.matdes.2016.05.035>
- [61] Zhong Y, Liu L, Wikman S, Cui D, Shen Z (2016) Intragranular cellular segregation network structure strengthening 316L stainless steel prepared by selective laser melting. *J Nucl Mater* 470:170–178. <https://doi.org/10.1016/j.jnucmat.2015.12.034>
- [62] Chao Q, Cruz V, Thomas S, Birbilis N, Collins P, Taylor A, Hodgson PD, Fabijanic D (2017) On the enhanced corrosion resistance of a selective laser melted austenitic stainless steel.

- Scr Mater 141:94–98. <https://doi.org/10.1016/j.scriptamat.2017.07.037>
- [63] Vrancken B, Thijs L, Kruth J-P, Van Humbeeck J (2012) Heat treatment of Ti6Al4V produced by Selective Laser Melting: microstructure and mechanical properties. *J Alloys Compd* 541:177–185. <https://doi.org/10.1016/j.jallcom.2012.07.022>
- [64] Yu H, Yang J, Yin J, Wang Z, Zeng X (2017) Comparison on mechanical anisotropies of selective laser melted Ti-6Al-4V alloy and 304 stainless steel. *Mater Sci Eng A* 695:92–100. <https://doi.org/10.1016/j.msea.2017.04.031>
- [65] Kunze K, Etter T, Grässlin J, Shklover V (2014) Texture, anisotropy in microstructure and mechanical properties of IN738LC alloy processed by selective laser melting (SLM). *Mater Sci Eng A* 620:213–222. <https://doi.org/10.1016/j.msea.2014.10.003>
- [66] Casati R, Lemke J, Vedani M (2016) Microstructure and fracture Behavior of 316L austenitic stainless steel produced by selective laser melting. *J Mater Sci Technol* 32:738–744. <https://doi.org/10.1016/j.jmst.2016.06.016>
- [67] Pourbabak S, Montero-Sistiaga ML, Schryvers D, Van Humbeeck J, Vanmeensel K (2019) Microscopic investigation of as built and hot isostatic pressed Hastelloy X processed by Selective Laser Melting. *Mater Charact* 153:366–371. <https://doi.org/10.1016/j.matchar.2019.05.024>
- [68] Liu Y, Zhang J, Pang Z (2018) Numerical and experimental investigation into the subsequent thermal cycling during selective laser melting of multi-layer 316L stainless steel. *Opt Laser Technol* 98:23–32. <https://doi.org/10.1016/j.optlastec.2017.07.034>
- [69] Bartolomeu F, Buciumeanu M, Pinto E, Alves N, Carvalho O, Silva FS, Miranda G (2017) 316L stainless steel mechanical and tribological behavior—A comparison between selective laser melting, hot pressing and conventional casting. *Addit Manuf* 16:81–89. <https://doi.org/10.1016/j.addma.2017.05.007>
- [70] Gorsse S, Hutchinson C, Gouné M, Banerjee R (2017) Additive manufacturing of metals: a brief review of the characteristic microstructures and properties of steels, Ti-6Al-4V and high-entropy alloys. *Sci Technol Adv Mater* 18:584–610. <https://doi.org/10.1080/14686996.2017.1361305>
- [71] Wright SI, Nowell MM, Field DP (2011) A review of strain analysis using electron backscatter diffraction. *Microsc Microanal* 17:316–329. <https://doi.org/10.1017/S1431927611000055>
- [72] Humphreys FJ, Hatherly M (2004) Recrystallization and related annealing phenomena. Elsevier Ltd. <https://doi.org/10.1017/CBO9781107415324.004>
- [73] Krog-Pedersen S, Bowen JR, Pantleon W (2009) Quantitative characterization of the orientation spread within individual grains in copper after tensile deformation. *Int J Mater Res* 100:433–438. <https://doi.org/10.3139/146.110032>
- [74] Field DP, Bradford LT, Nowell MM, Lillo TM (2007) The role of annealing twins during recrystallization of Cu. *Acta Mater* 55:4233–4241. <https://doi.org/10.1016/j.actamat.2007.03.021>
- [75] Xu W, Quadir MZ, Ferry M (2009) A high-resolution three-dimensional electron backscatter diffraction study of the nucleation of recrystallization in cold-rolled extra-low-carbon steel. *Metall Mater Trans A Phys Metall Mater Sci* 40:1547–1556. <https://doi.org/10.1007/s11661-009-9873-6>
- [76] Miller VM, Johnson AE, Torbet CJ, Pollock TM (2016) Recrystallization and the development of abnormally large grains after small strain deformation in a polycrystalline nickel-based superalloy. *Metall Mater Trans A Phys Metall Mater Sci* 47:1566–1574. <https://doi.org/10.1007/s11661-016-3329-6>
- [77] Woo W, Jeong JS, Kim D, Lee CM, Choi S, Suh J, Lee SY, Harjo S (2020) Stacking fault energy analyses of additively manufactured stainless steel 316L and CrCoNi medium entropy alloy using in situ neutron diffraction. *Sci Rep*. 1-0:1350. <https://doi.org/10.1038/s41598-020-58273-3>
- [78] Choi JP, Shin GH, Brochu M, Kim YJ, Yang SS, Kim KT, Yang DY, Lee CW, Yu JH (2016) Densification behavior of 316L stainless steel parts fabricated by selective laser melting by variation in laser energy density. *Mater Trans* 57:1952–1959. <https://doi.org/10.2320/matertrans.M2016284>
- [79] Michiuchi M, Kokawa H, Wang ZJ, Sato YS, Sakai K (2006) Twin-induced grain boundary engineering for 316 austenitic stainless steel. *Acta Mater* 54:5179–5184. <https://doi.org/10.1016/j.actamat.2006.06.030>
- [80] Tomota Y, Ojima M, Harjo S, Gong W, Sato S, Ungár T (2019) Dislocation densities and intergranular stresses of plastically deformed austenitic steels. *Mater Sci Eng A* 743:32–39. <https://doi.org/10.1016/j.msea.2018.09.052>
- [81] Aota LS, Bajaj P, Zilnyk KD, Ponge D, Sandim HRZ (2021) The origin of abnormal grain growth upon thermomechanical processing of laser powder-bed fusion alloys. *Materialia* 20:101243. <https://doi.org/10.1016/j.mtla.2021.101243>
- [82] Haessner F (1978) Recrystallization of metallic materials. Riederer-Verlag GmbH, Stuttgart
- [83] Garlea E, Choo H, Sluss CC, Koehler MR, Bridges RL, Xiao X, Ren Y, Jared BH (2019) Variation of elastic mechanical properties with texture, porosity, and defect characteristics in laser powder bed fusion 316L stainless steel. *Mater Sci Eng A* 763:138032. <https://doi.org/10.1016/j.msea.2019.138032>

- [84] Manohar PA, Ferry M, Chandra T (1998) Five decades of the Zener equation. *ISIJ Int* 38:913–924. <https://doi.org/10.2355/isijinternational.38.913>
- [85] Humphreys FJ, Hatherly M (2004) *Recrystallization and related annealing phenomena*, 2nd edn. Elsevier, Pittsburgh
- [86] Varin RA (1984) Grain boundary diffusion and free energy during the recrystallization of type 316 stainless steel. *Mater Sci Eng* 66:97–105. [https://doi.org/10.1016/0025-5416\(84\)90144-7](https://doi.org/10.1016/0025-5416(84)90144-7)
- [87] Martin JW, Doherty RD, Cantor B (1997) *Stability of microstructure in metallic systems*. Cambridge University Press, Cambridge
- [88] Herzig C, Mishin Y (2005) Grain boundary diffusion in metals. In: Heitjans P, Kärger J (eds) *Diffus Condens Matter Methods Mater Model*. Springer, Berlin
- [89] Kirchner HOK (1971) Coarsening of grain-boundary precipitates. *Metall Trans* 2:2861–2864. <https://doi.org/10.1007/BF02813264>
- [90] Hemmasian Etefagh A, Guo S (2018) Electrochemical behavior of AISI316L stainless steel parts produced by laser-based powder bed fusion process and the effect of post annealing process. *Addit Manuf* 22:153–156. <https://doi.org/10.1016/j.addma.2018.05.014>
- [91] Wei HL, Mazumder J, DebRoy T (2015) Evolution of solidification texture during additive manufacturing. *Sci Rep* 5:16446. <https://doi.org/10.1038/srep16446>
- [92] Choo H, Sham KL, Bohling J, Ngo A, Xiao X, Ren Y, Depond PJ, Matthews MJ, Garlea E (2019) Effect of laser power on defect, texture, and microstructure of a laser powder bed fusion processed 316L stainless steel. *Mater Des* 164:107534. <https://doi.org/10.1016/j.matdes.2018.12.006>
- [93] Pham MS, Dovggy B, Hooper PA, Gourlay CM, Piglione A (2020) The role of side-branching in microstructure development in laser powder-bed fusion. *Nat Commun* 11:1–12. <https://doi.org/10.1038/s41467-020-14453-3>
- [94] Chowdhury SG, Das S, Ravikumar B, De PK (2006) Twinning-induced sluggish evolution of texture during recrystallization in AISI 316L stainless steel after cold rolling. *Metall Mater Trans A Phys Metall Mater Sci* 37:2349–2359. <https://doi.org/10.1007/BF02586209>
- [95] Liu Y, Militzer M, Perez M (2019) Phase field modelling of abnormal grain growth. *Materials (Basel)* 12:4048–4068
- [96.] Huang W, Yuan S, Chai L, Jiang L, Liu H, Wang F, Wang D, Wang J (2019) Development of grain boundary character distribution in medium-strained 316L stainless steel during annealing. *Met Mater Int* 25:364–371. <https://doi.org/10.1007/s12540-018-0203-7>

**Publisher's Note** Springer Nature remains neutral with regard to jurisdictional claims in published maps and institutional affiliations.